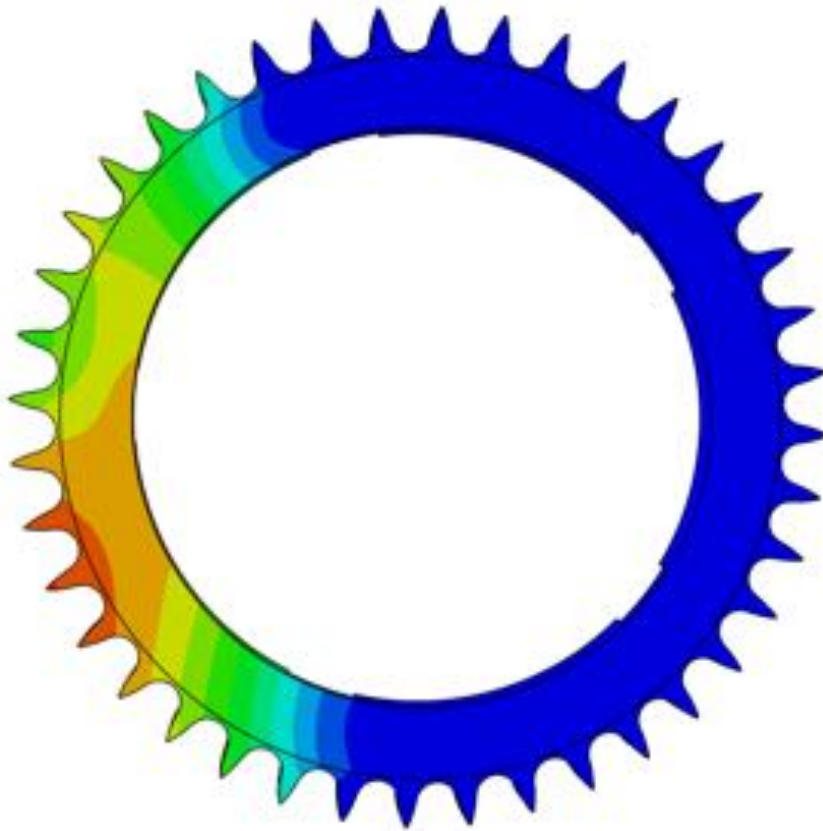


ME 461:
Finite Element
Analysis

Fall | 2015



A Semester Report on:

Finite Element Analysis of a Bicycle

Group Members:

Christopher Kozuch, Ian Hanna, Savannah Messenger,
and Travis Carroll



PennState
College of Engineering

Table of Contents

Table of Contents	2
Executive Summary	3
Acknowledgements	4
Section 1: Background and Project Plan	5
Section 2: Development and Description of CAD Geometry	7
Section 3: Development of Finite Element Meshes	11
Section 4: Development and Description of the Model Assembly and Boundary Conditions .	24
Section 5: Analysis of Finite Element Model	28
Simulations were run using static analysis on 16 processors each in Abaqus CAE.	
Section 6: Additional Analysis of Frame	43
Section 7: Summary of Major Findings	48
Section 8: Works Cited	50

Executive Summary

This report endeavors to highlight possible design improvements for the modern bicycle using finite element analysis. This process was broken down into six distinct steps. These steps are summarized below.

The first step was to conduct background research and develop a constitutive model. The background research revealed that while some analysis had been carried out in the past, the cases studied were mostly extreme events, and few design changes had been suggested. The constitutive model was developed for linear solid mechanics using force balances and extended Hooke's Law.

Once that was complete, useful CAD geometries for the development of models had to be obtained. These geometries were procured from open-source sites, and they detail the frame, drive train (pedal, crank, and gear), brakes, and wheels. The frame and drive train were determined to be the most crucial, so work was discontinued for the others.

Next, meshes were produced for the various geometries. The mesh sizes were tailored to achieve the best balance between accuracy and computational efficiency. The result was 11,504 elements for the frame, 52,902 elements for the gear, 16,637 elements for the pedal, and 154,106 elements for the crank. The element count for the crank was highest because it is the largest, and the element count for the gear was driven up by the sharp geometry at the teeth tips.

The fourth step was to create the assembly models and boundary conditions. These were determined by researching common materials for bicycle construction and studying the literature on loads applied during normal use of a bicycle. These values were then translated into the effects they would have on each component.

Once the assembly models were completed, the simulations were run using static analysis on 16 processors each using Abaqus CAE. The resulting maximum stresses, strains, and displacements were then recorded and analyzed. Additional analysis was performed for the frame, including modal and dynamic analysis. These values were then used to make design suggestions in the final step.

The sixth and final step produced three major conclusions. The first is that variations in the frame tubing reduce the structural efficiency. The second is that the attachment system between the gear and the crank introduces unnecessary stresses, and the third is that an integrated shaft for the pedal could improve durability.

It is our team's hope that this analysis and the resulting design conclusions will allow for the construction of more durable and efficient bicycles. Our future work will focus both on the simulation of more dynamic events, such as collisions, as well as those areas of the bicycle that we excluded, like the brakes and tires.

Acknowledgements

Our team would like to acknowledge all of the guidance and help that Dr. Kraft has provided us. We would also like to thank the Penn State Institute for Cyberscience for allowing us to use their high performance computing clusters and software.

Section 1: Background and Project Plan

Our objective is to model various components of a generic bicycle. The aim is to calculate stress and strain under normal use conditions.

Last year, the number of bicycle riders in the United States rose to an all-time high of 67.33 million [1]. Given that there are 318.4 million people in the United States [2], this means that more than one fifth of the population uses bicycles. With such a large user pool, it is surprising that the average consumer bicycle has remained relatively unchanged for the past 50 years. To help push this technology forward, our team has decided to perform a comprehensive mechanical analysis of the modern consumer bicycle. It is our hope that a deeper understanding of the mechanics involved in general use will provide the basis for new technology development.

The majority of past bicycle analyses focus on the bicycle frame. We will use these to benchmark our work and ensure accuracy. One such study by Arola et. al. conducted experimental tests on a frame that is highly similar to our bicycle model. Figure 1 shows the frame that was used in the experimental study [3].

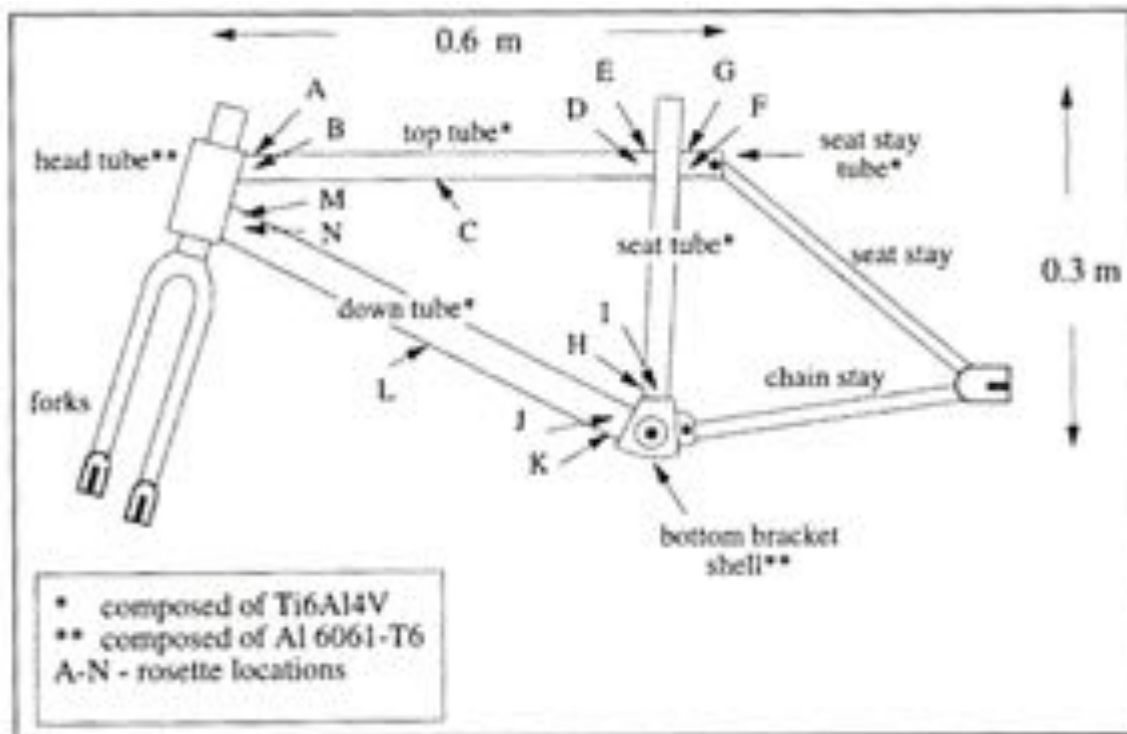


Figure 1: Frame used in 1999 Experimental Study

In this study, the frame was fitted with 14 strain rosettes (locations are shown in Figure 1). The bicycle was tested dynamically, which included moderately-sized jumps with mainly rear-tire landing and larger jumps with mainly front-tire landing. The highest stresses were found at rosette N when the bike underwent larger jumps with mainly front-tire landing. These stresses were measured to be close to 400.0 MPa [3].

In addition to the experimental study, our group also examined a study of a bicycle frame using FEA completed in 2014. This study subjected the bicycle frame to multiple loading conditions. The greatest stresses in the frame occurred when the bike was subjected to the “horizontal impact” loading conditions. These loading conditions were meant to simulate a low-speed, head-on collision with a wall or curb. The maximum stress under these conditions was around 24.0 MPa and this occurred in the top, horizontal tube of the bicycle frame [4].

As mentioned above, our model is not limited to only the frame. The following report details the analysis of both the frame and drive train, which includes the pedal, crank, and gear. These elements were subjected to normal use conditions and the results are presented below.

Since the model will be limited to solid mechanics, the number of constitutive equations required is relatively small. The first, shown below, is the force balance. The displacement is given by \mathbf{u} , the stress tensor is given by $\boldsymbol{\sigma}$, the body forces are given by \mathbf{b} , and the density is given by ρ .

$$\nabla \cdot \boldsymbol{\sigma} + \mathbf{b} = \rho \ddot{\mathbf{u}} \quad (1-1)$$

In addition to the force balance equation, the extended Hooke’s law is required to describe the relationship between stress and strain. Poisson’s ratio is given by ν , the strain is given by $\boldsymbol{\varepsilon}$, the shear strain is given by $\boldsymbol{\gamma}$, Young’s modulus is given by E , and the stress is given by $\boldsymbol{\sigma}$.

$$\begin{aligned} \varepsilon_{11} &= \frac{1}{E} [\sigma_{11} - \nu(\sigma_{22} + \sigma_{33})] \\ \varepsilon_{22} &= \frac{1}{E} [\sigma_{22} - \nu(\sigma_{11} + \sigma_{33})] \\ \varepsilon_{33} &= \frac{1}{E} [\sigma_{33} - \nu(\sigma_{11} + \sigma_{22})] \end{aligned} \quad (1-2)$$

$$\tau_{12} = \frac{\gamma_{12}}{G}, \tau_{23} = \frac{\gamma_{23}}{G}, \tau_{31} = \frac{\gamma_{31}}{G}, G = \frac{E}{2(1-\nu)}$$

Section 2: Development and Description of CAD Geometry

The majority of the CAD model was derived from open source material. This helped reduce lead time and increase component accuracy. However, select components were modified or completely custom built to assure strong mesh properties. Please note that all engineering drawings are shown in inches. For meshing and analysis, the models were scaled to SI units.

Frame

The CAD geometry for the frame was obtained from [5]. An engineering drawing and exploded view are shown respectively in Figure 2 and Figure 3.

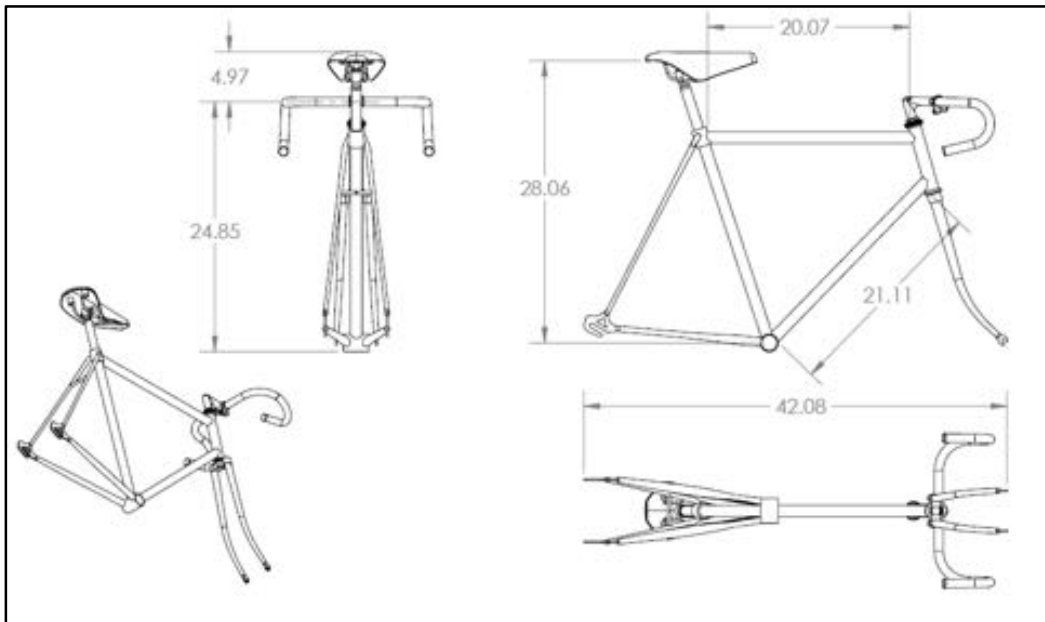


Figure 2: Engineering Drawing for Frame



Figure 3: Exploded View of Frame

Wheel

Like the frame, the CAD geometry for the wheel was obtained from [5]. An engineering drawing and model view are shown respectively in Figure 4 and Figure 5.

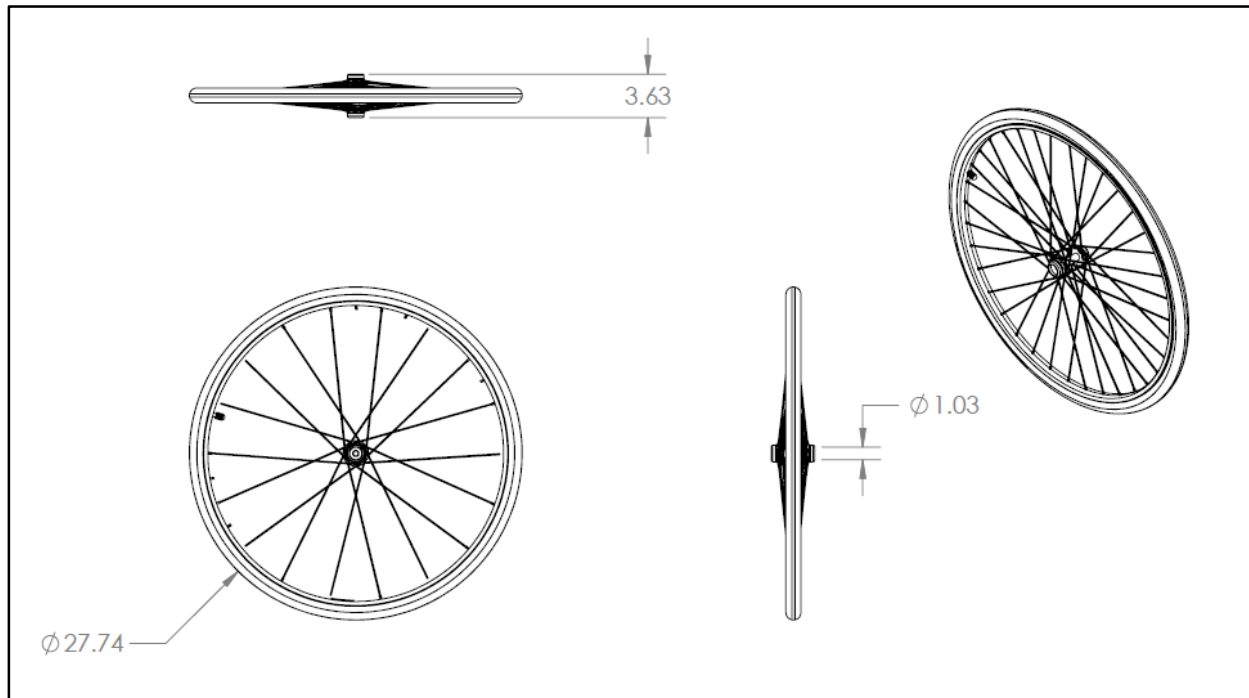


Figure 4: Engineering Drawing for Wheel

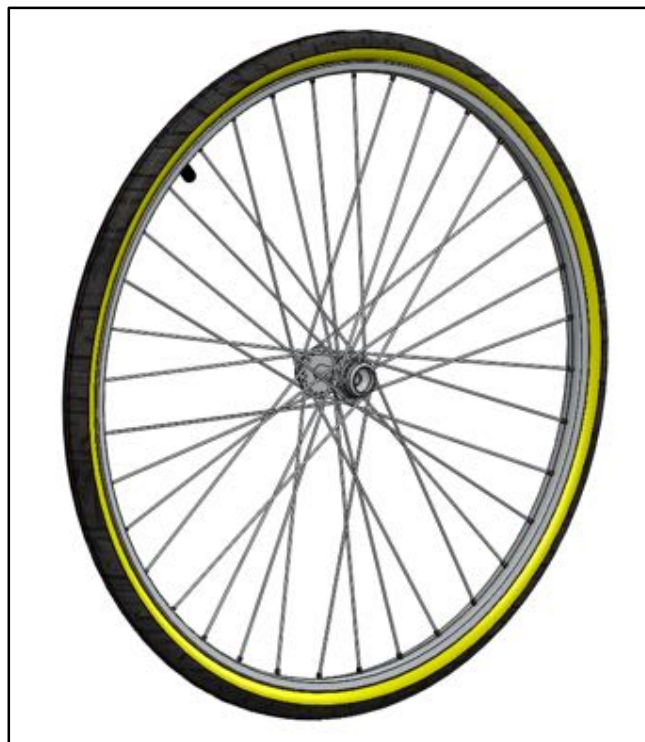


Figure 5: Model View of Wheel

Drive Train

An original model was created for the drive train in order to have finer control over the model. This will allow for efficient geometry refinement, which will produce a better mesh. The design and dimensions are based on the Chinese Flying Pigeon because it is the most popular bicycle in the world [6]. Only one gear has been retained because the others are not load-bearing and represent significant computational expense. Engineering drawings and an exploded view of the model are presented below in Figure 6 and Figure 7.

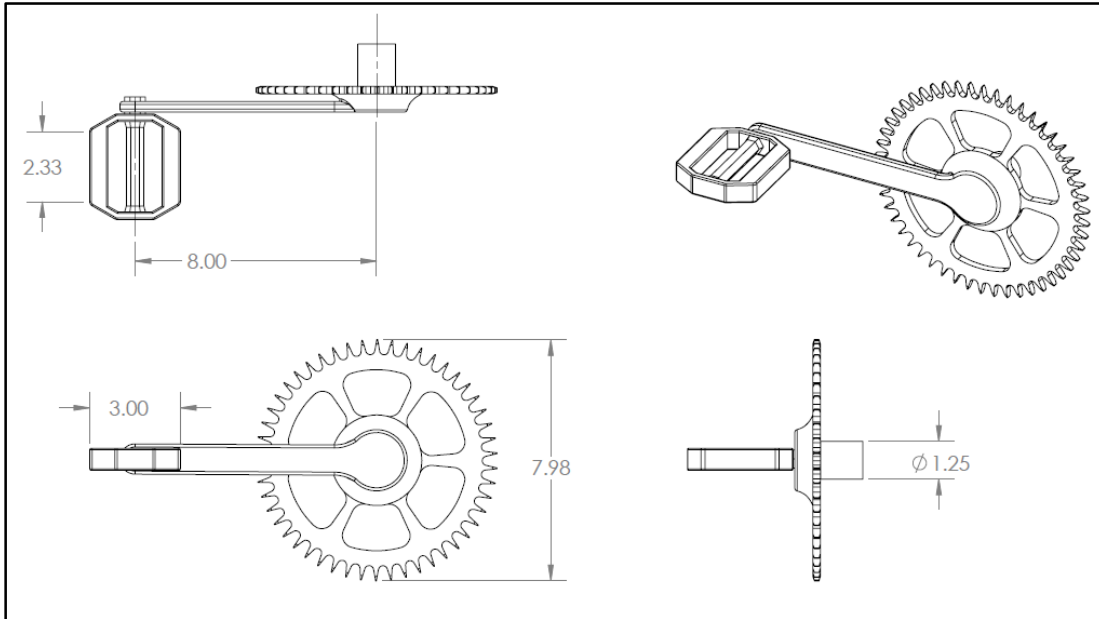


Figure 6: Engineering Drawing for Crankset and Pedal

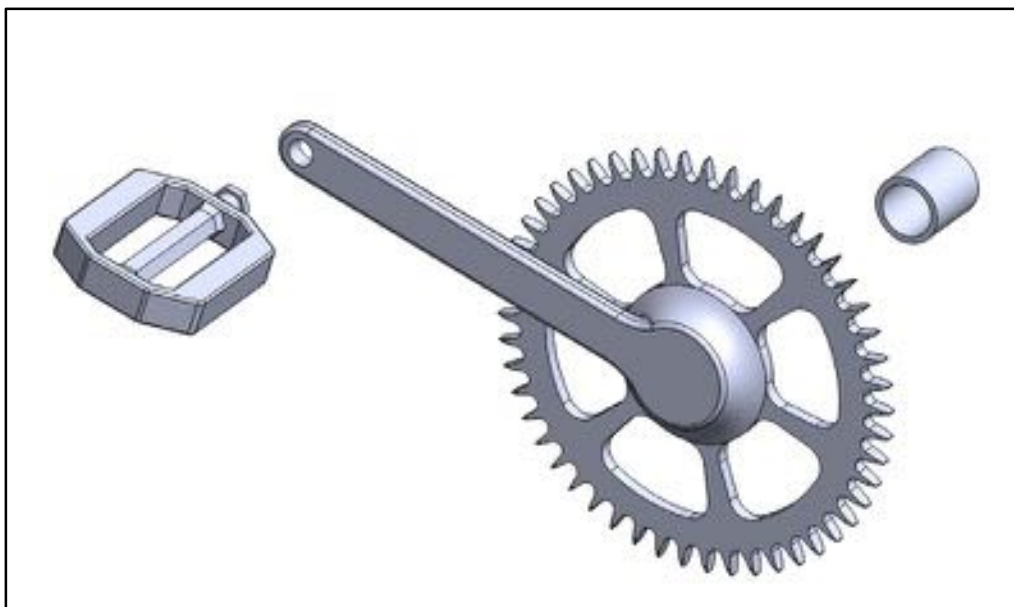


Figure 7: Exploded View of the Crankset and pedal

Section 3: Development of Finite Element Meshes

The initial proposal was reduced in an effort to control labor commitment. For the following sections, only the frame, gear, crank, and pedal will be considered.

Frame

The basic geometry of the frame (shown in Figure 10) is not very complex, but it is thin (because the tubes are hollow) and has some sharp points where the parts are connected. A detailed view of one of these attachment points is shown in Figure 11. The thin edges of the tubes drive down the element size.

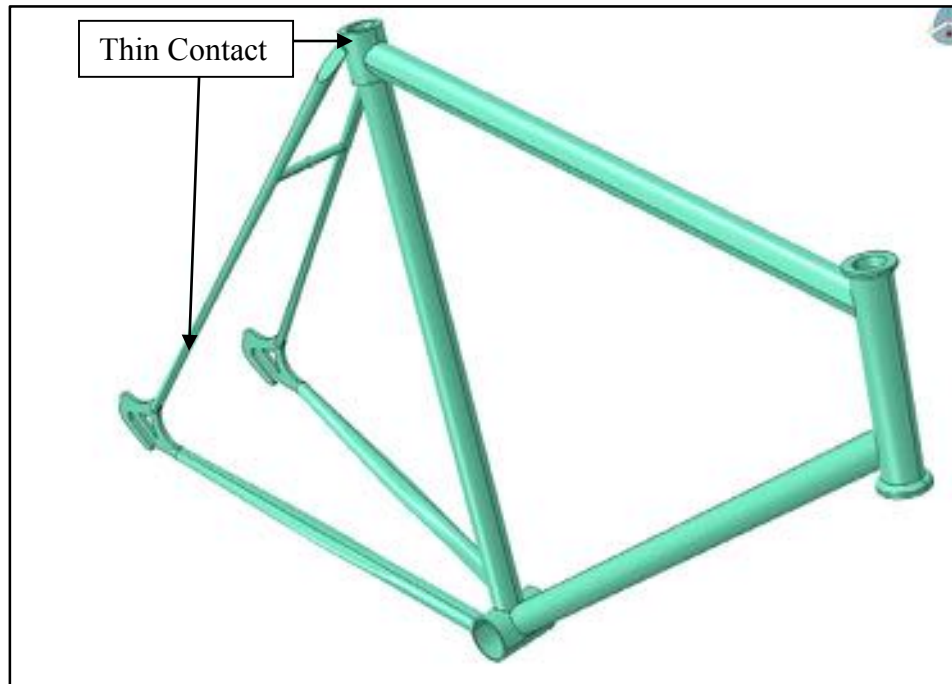


Figure 10: STEP Model of frame

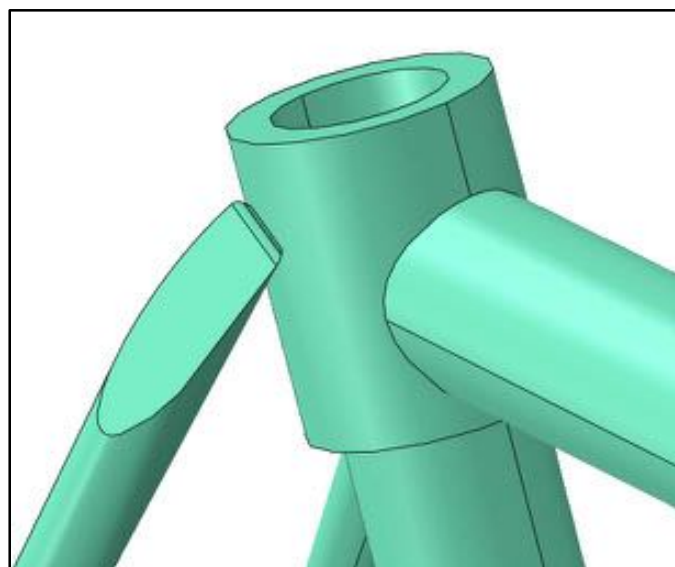


Figure 11: Detail View of Seat Attachment Point

Procedure

To mesh the frame, a SolidWorks model was converted to a STEP file and then imported into Abaqus using a scaling factor of .0254 to convert from inches to meters. The material properties for Al 6061-T6 (given in Table 1) were then assigned. The calculated mass for the frame was 4.52 kg. The mass is reasonable for a hollow aluminum frame. Next, a section was created for the material. A dependent assembly instance was formed from this section. The mesh was generated using the following parameters: automatic, quadratic, tetrahedral, and a global size of 0.005.

Results

The meshed part is shown in Figure 12. This model has a total of 11,504 elements. The mesh quality is relatively good, however, the connection points have sharp geometry, which produced poor elements. The poor elements are highlighted in Figure 13 and Figure 14. The edges of all elements are relatively equal. Less than .058% of the elements have an aspect ratio greater than 10. The average aspect ratio is 1.82 and less than .054% of the faces have an angle less than 5 degrees. Figure 15 and Figure 16 show view cuts of the frame mesh.



Figure 12: Full Frame Mesh



Figure 13: Poor Elements in Frame

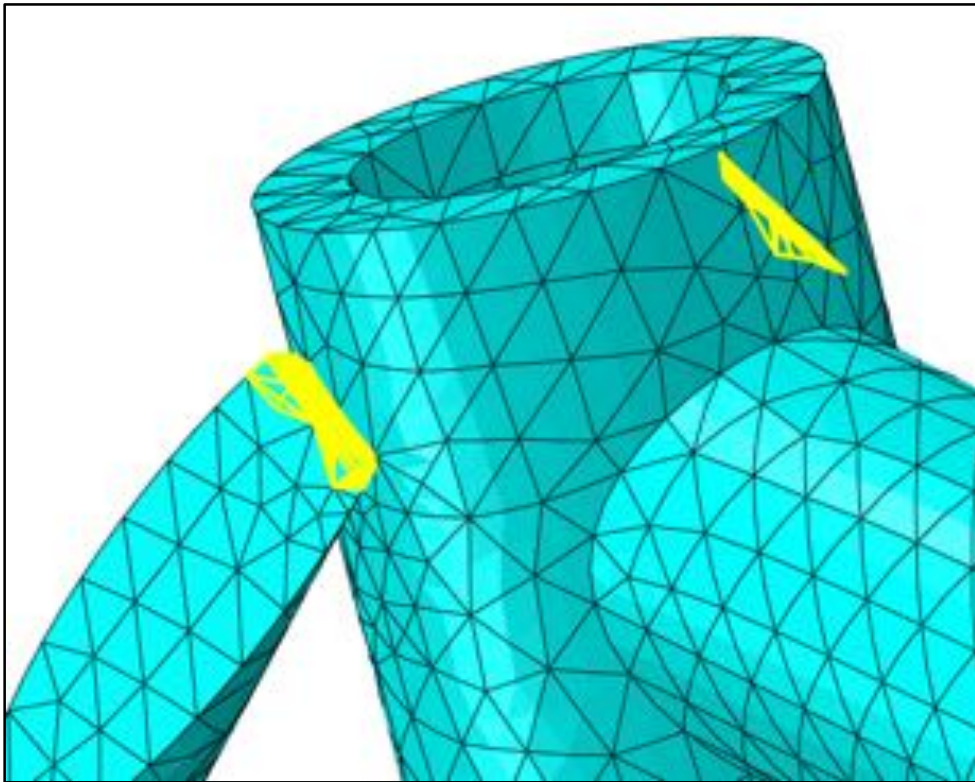


Figure 14: Detail View of Poor Elements near Seat Attachment

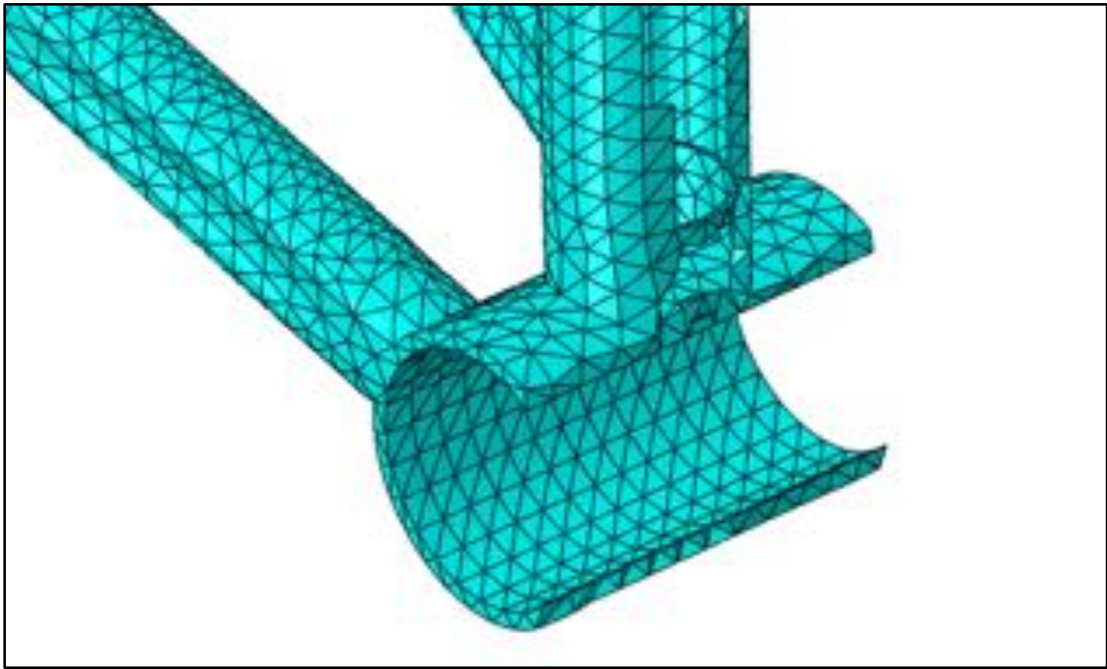


Figure 15: Vertical Cut of Frame Mesh



Figure 16: Horizontal Cut of Frame Mesh

Gear

Compared to some of the other components, the geometry of the gear is relatively simple. It is basically a toothed hoop with connection grooves. However, the small radii on the teeth tips force the element size down. Additionally, a very thin rim surrounds the inner diameter, which drives the element size down even farther. As a result, the gear has a very high element count.

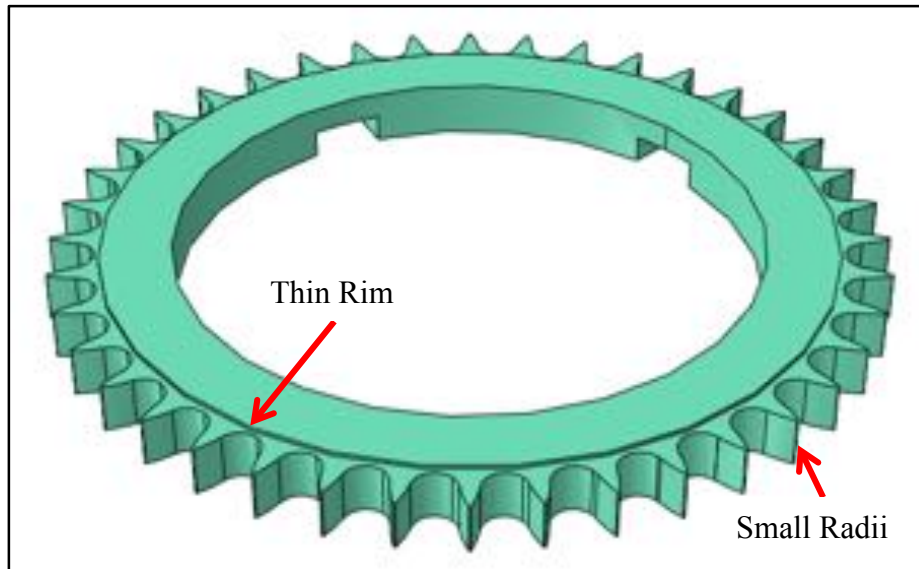


Figure 17: STEP Model for Gear

Procedure

Meshing the gear was achieved through several steps. First, the CAD model was imported as STEP file into Abaqus with a scaling factor of 0.001 to convert from millimeters to meters. Then the material was created. Al 7075-T6 was used for this model, and the material properties are given in Table 2. The calculated mass was 0.492 kg, which is reasonable for a low weight metal like Al 7075-T6. Next, a section was created then assigned to the model. A dependent assembly instance was then created using that section. Finally, an automatic, quadratic, tetrahedral mesh with global size of 0.001 was generated.

Results

Figure 18 shows the total resulting mesh. As mentioned above, the small feature sizes force small elements, so the number of elements is relatively high. This model has a total of 52,902 elements. Figure 19 shows a close-up of the mesh on the teeth.

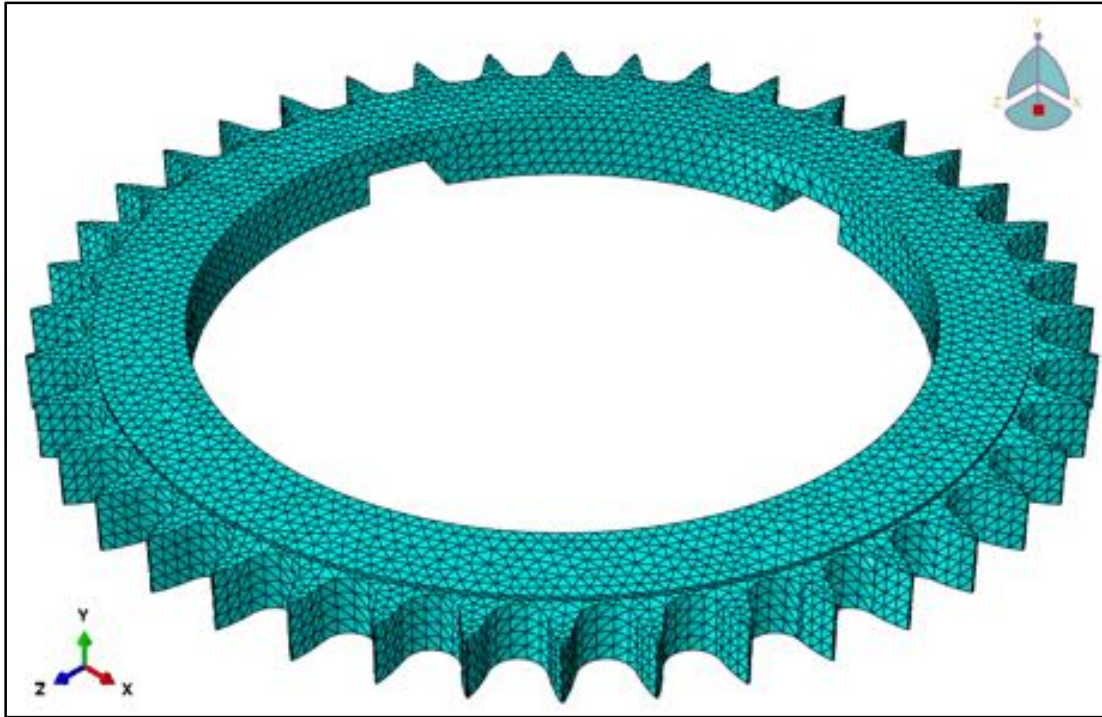


Figure 18: Full Mesh for Gear

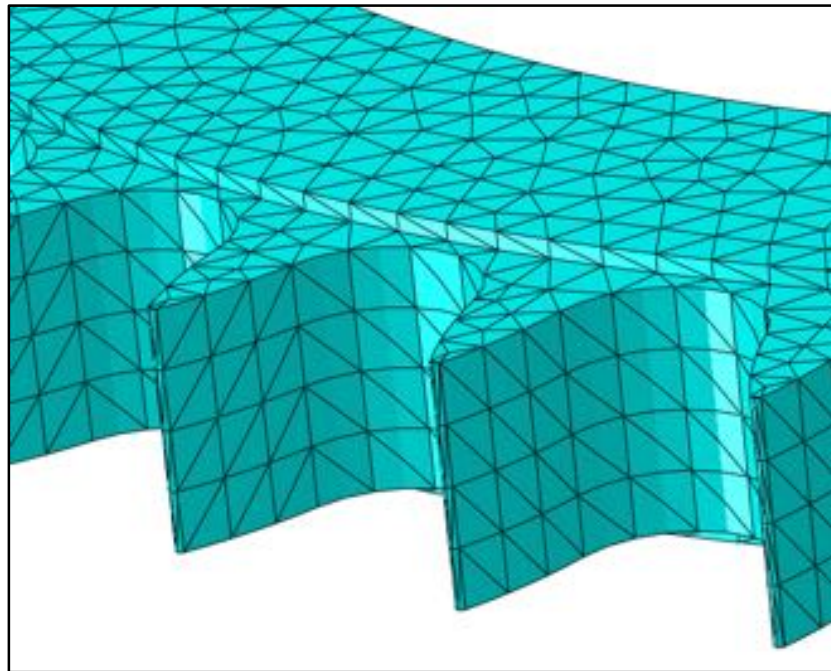


Figure 19: Detail View of Tooth Mesh

Figure 20 highlights the areas where there are low quality elements. As expected the low quality elements are mostly on teeth tips because they have very small radii. However, there are also some poor quality elements on the interior of the hoop. Overall, the mesh has fairly good quality. Less than 1.4% of the elements have an aspect ratio over 10, the average aspect ratio is 2.05, and less than 1.1% of the faces have an angle less than 5 degrees. Figure 21 and Figure 22 show cut-views of the mesh.

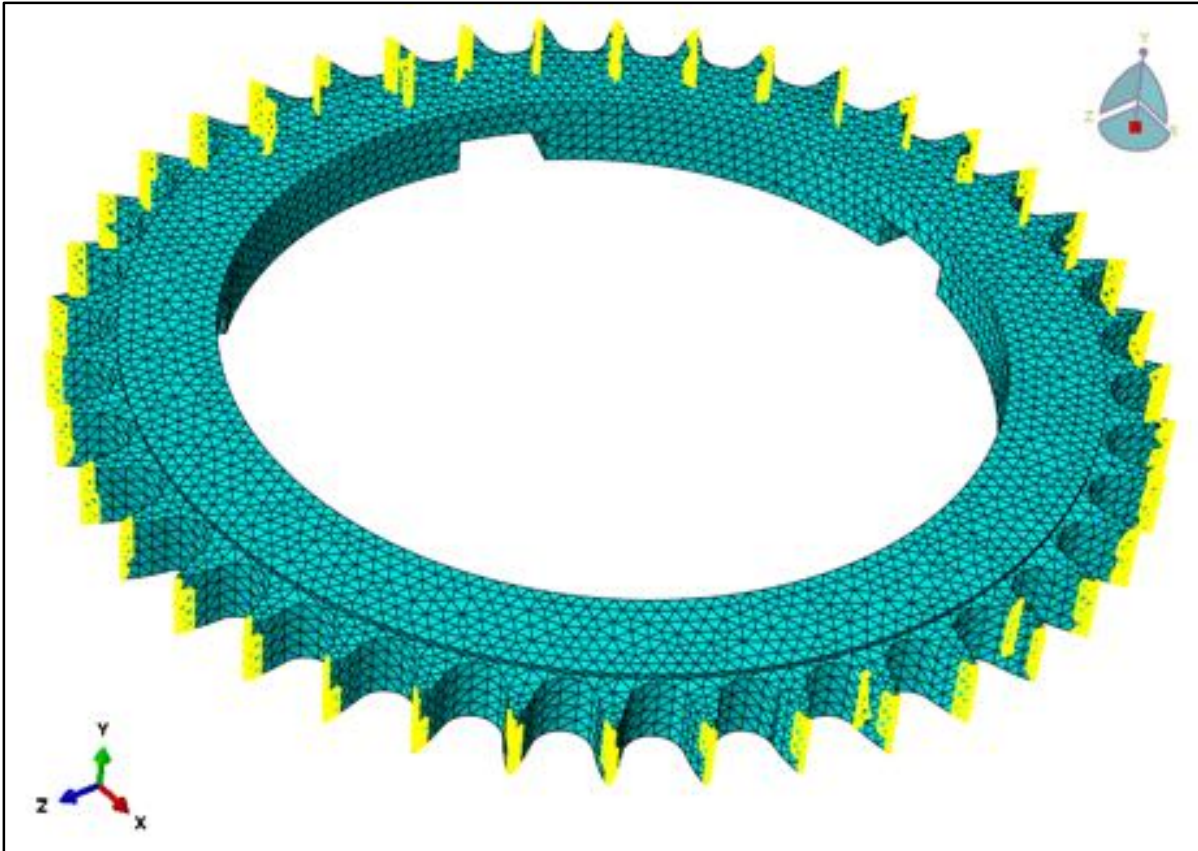


Figure 20: Poor Elements Highlighted

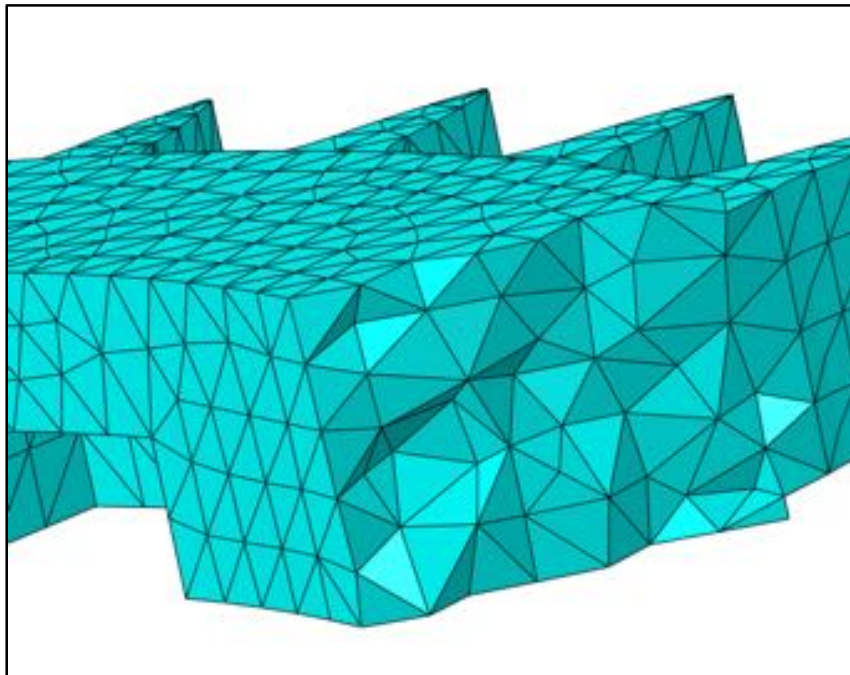


Figure 21: Vertical Cut for Gear Mesh

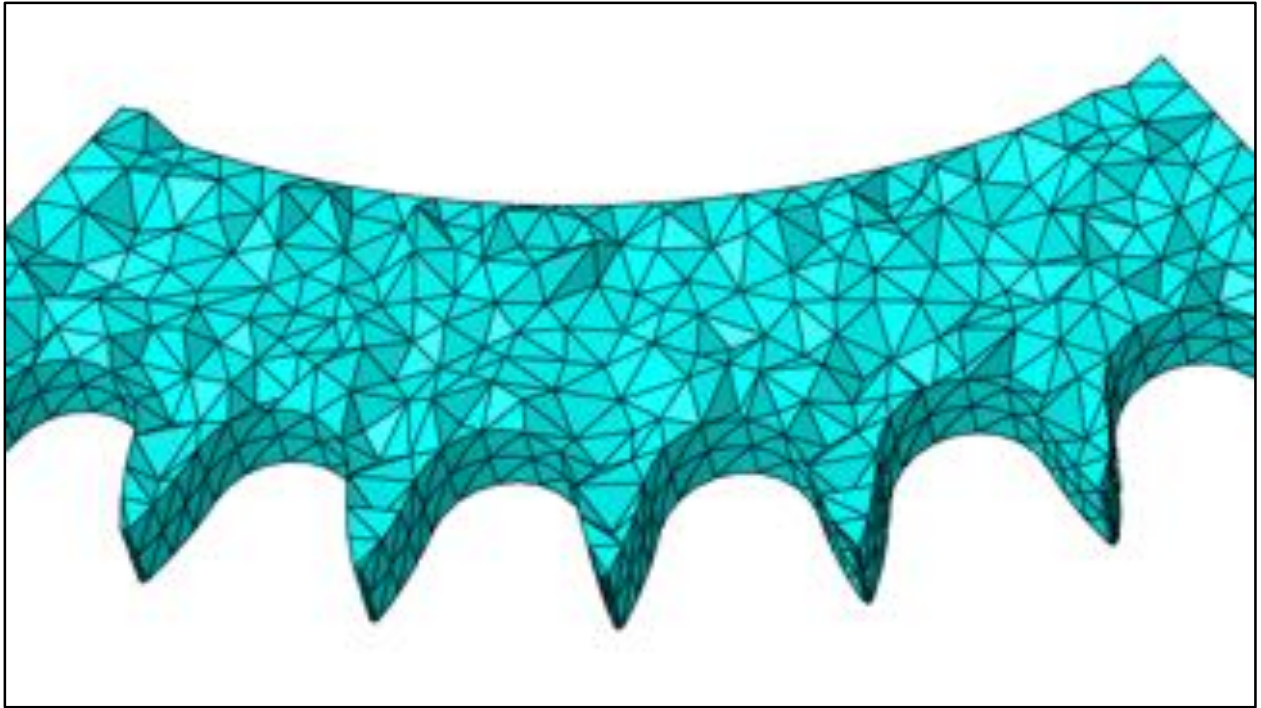


Figure 22: Horizontal Cut for Gear Mesh

Pedal

The pedal has a relatively simple geometry with a plane of symmetry about its centerline. However, there are geometric areas, specifically around the connection rod, that could cause high stress concentrations when a load is applied. These areas will require much higher element counts than the other areas.

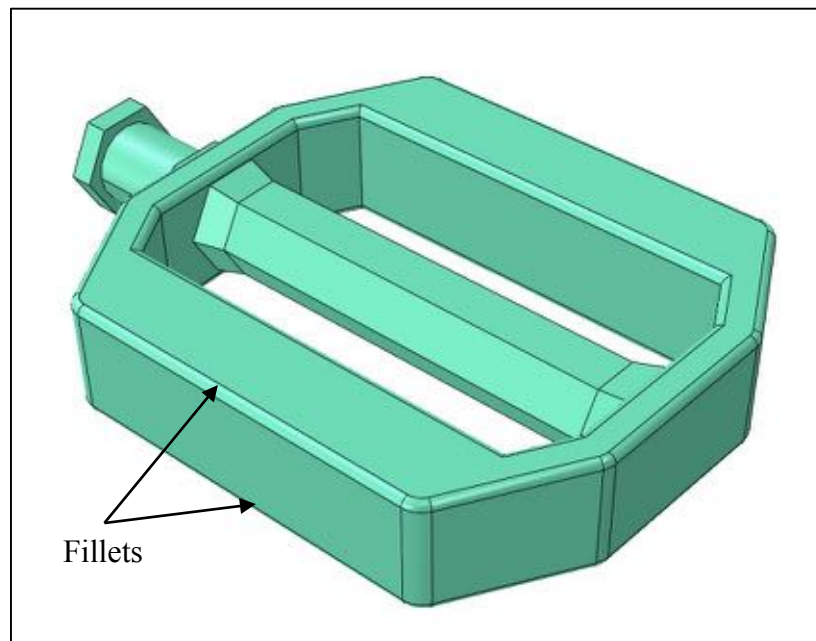


Figure 23: STEP Model for Pedal

Procedure

In order to mesh the pedal, the CAD geometry was imported as a STEP file into Abaqus. Next, a section with the material properties of Al 7075-T6 was created for the part geometry. The mass of the section was found to be 0.185 kg, which makes sense for a small part such as this. Once that was complete, a dependent assembly was constructed using just the section described above. Finally, an automatic tetrahedral, quadratic mesh was generated with a global mesh size of 0.0034.

Results

Figure 24 shows the full mesh of the bicycle pedal. There are significantly smaller tetrahedral elements around the edges of the pedal, where the geometry incorporates fillets. Overall, there are 16,637 elements.

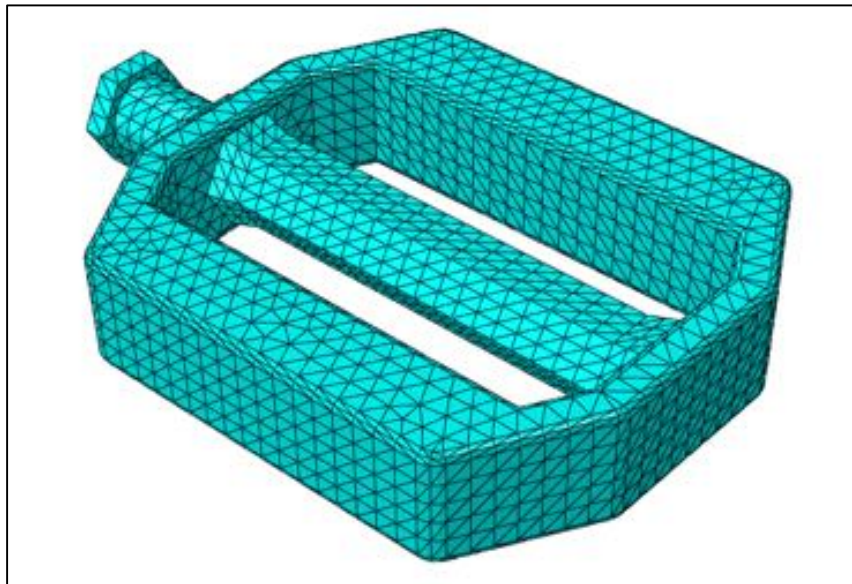


Figure 24: Full Pedal Mesh

As expected, most of the problem elements are located where the pedal meets the axle. There are a few other problem elements on the fillets of the pedal as well. These problem elements are highlighted in Figure 25. Overall, the mesh quality is good. Less than 0.085% of the elements have an aspect ratio greater than 10, less than 0.144% of the faces have an angle that is less than 5 degrees, and the average shape factor is 0.623. Figure 26 and Figure 27 show cut views of the mesh.



Figure 25: Problem Elements in the Mesh

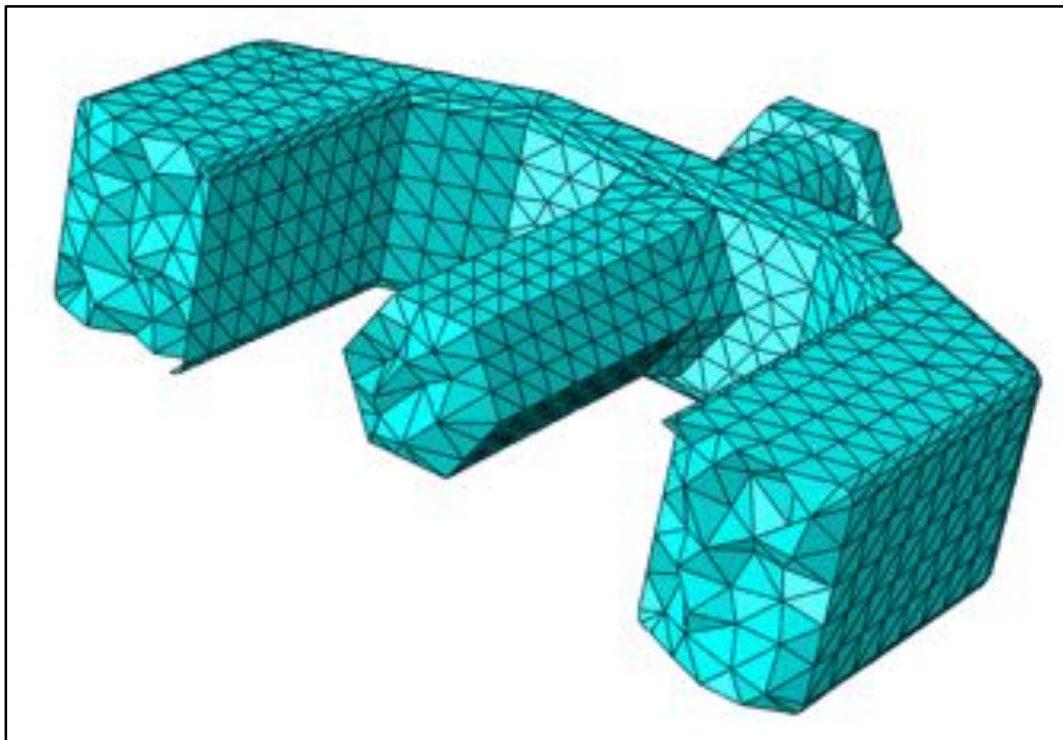


Figure 26: Vertical Cut for Pedal Mesh

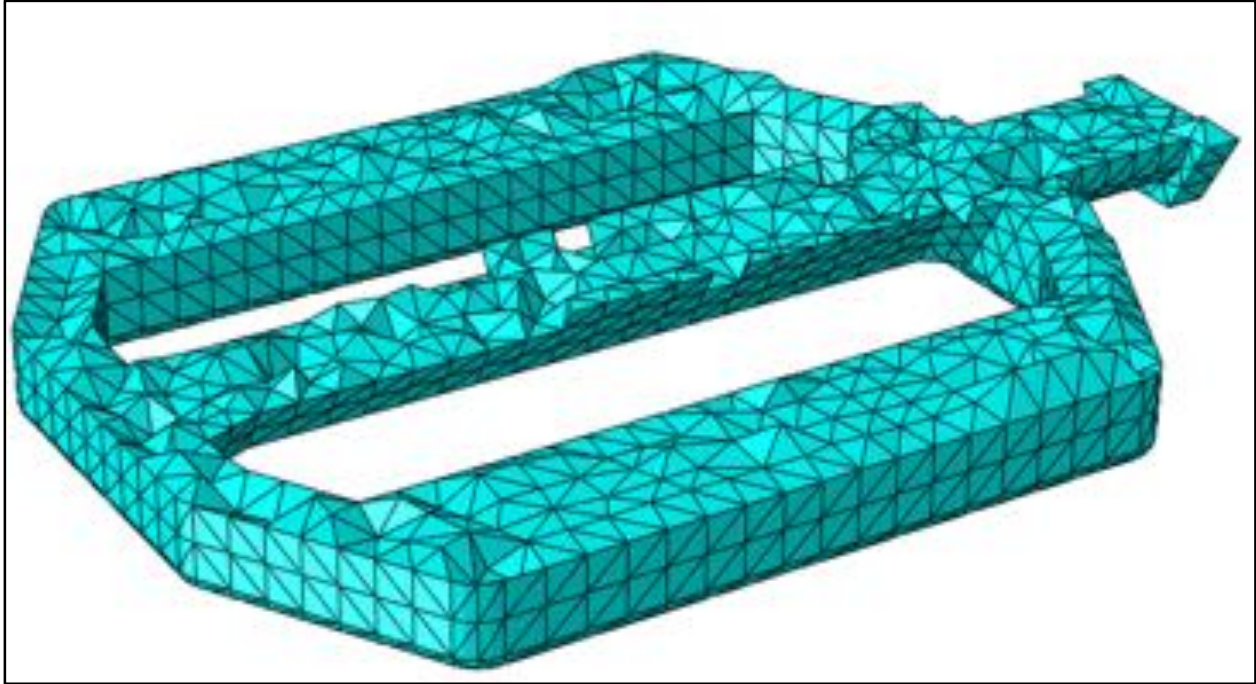


Figure 27: Horizontal Cut for Pedal Mesh

Crank Arm

The crank arm consists of five “spokes” located at the end of an arm with a rectangular cross section. At the opposite end of the arm, there is a hole that is used to attach the pedal. This is shown in Figure 28. Small fillets have forced the element size down to retain good element shape.

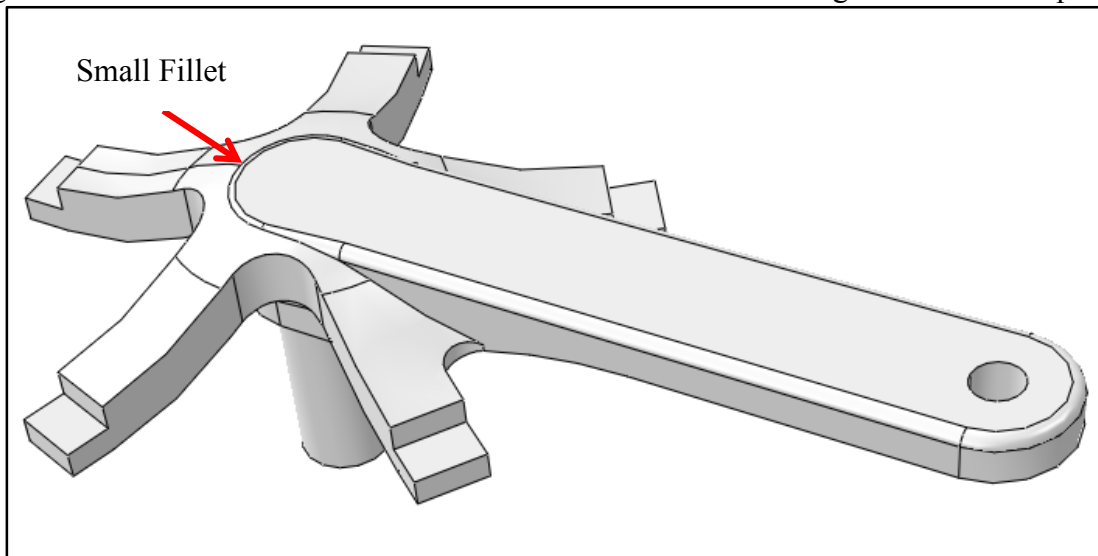


Figure 28: STEP Model of Crank Arm

Procedure

To mesh the crank arm, part geometry was converted to a STEP file and then imported into Abaqus. During the importing, a scaling factor of 0.001 was used to convert from millimeters to meters. A section was created using the imported geometry, and the same material as the gear and pedal, Al 7075, was assigned to it. The mass for the crank was calculated to be 4.03 kg, which is

reasonable for a solid aluminum part. A dependent assembly instance was then constructed using only this section. Finally, the mesh was generated using the following parameters: automatic, quadratic, tetrahedral, and a global size of 0.0025. A local size of 0.001 was applied to the small fillets.

Results

The meshed part is shown in Figure 29. This model has a total of 154,106 elements. The mesh quality is relatively good. None of the elements have an aspect ratio greater than 10, and only 3 elements (less than 0.002%) have angles less than 5 degrees. Additionally, none have a geometric deviation factor greater than 0.2. Poor quality elements are highlighted in Figure 30.



Figure 29: Full Mesh

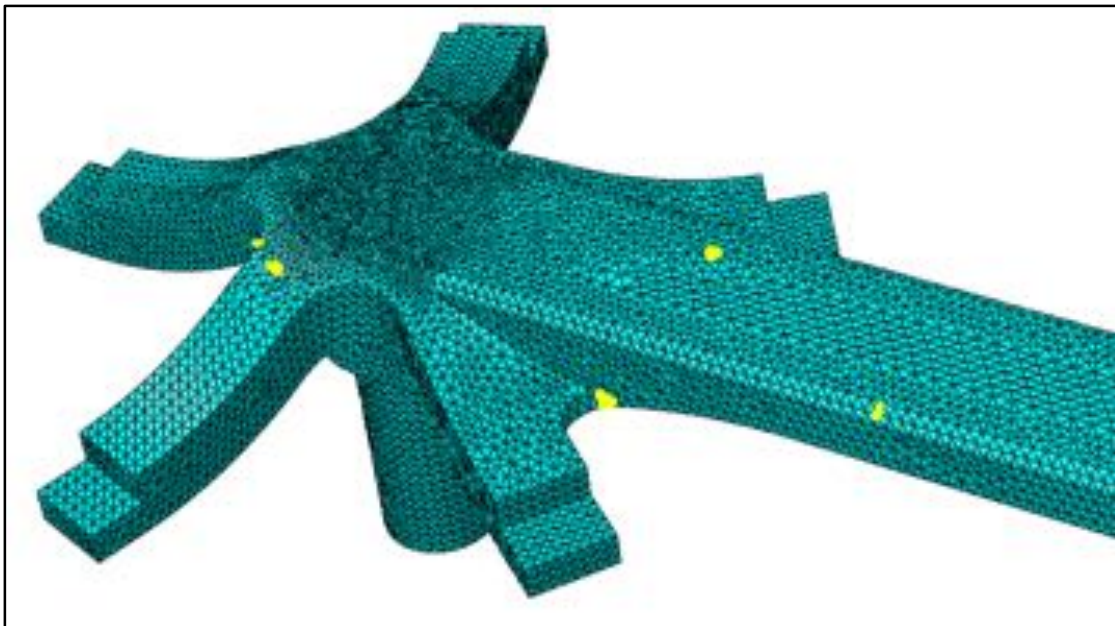


Figure 30: Poor Elements Highlighted for Crank Mesh

Figure 31 and Figure 32 show view cuts of the crank mesh. As mentioned above, the mesh size was reduced for areas where small fillets were present.

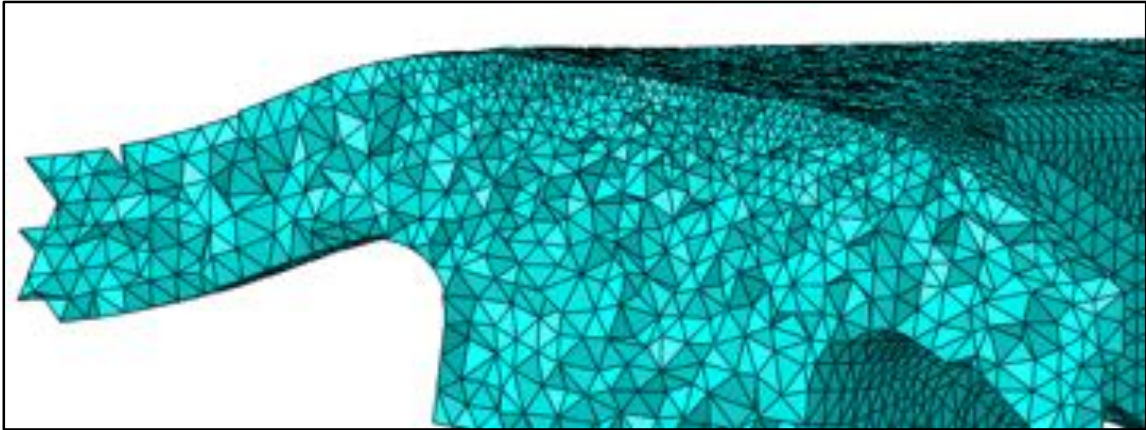


Figure 31: Vertical Cut for Crank Mesh

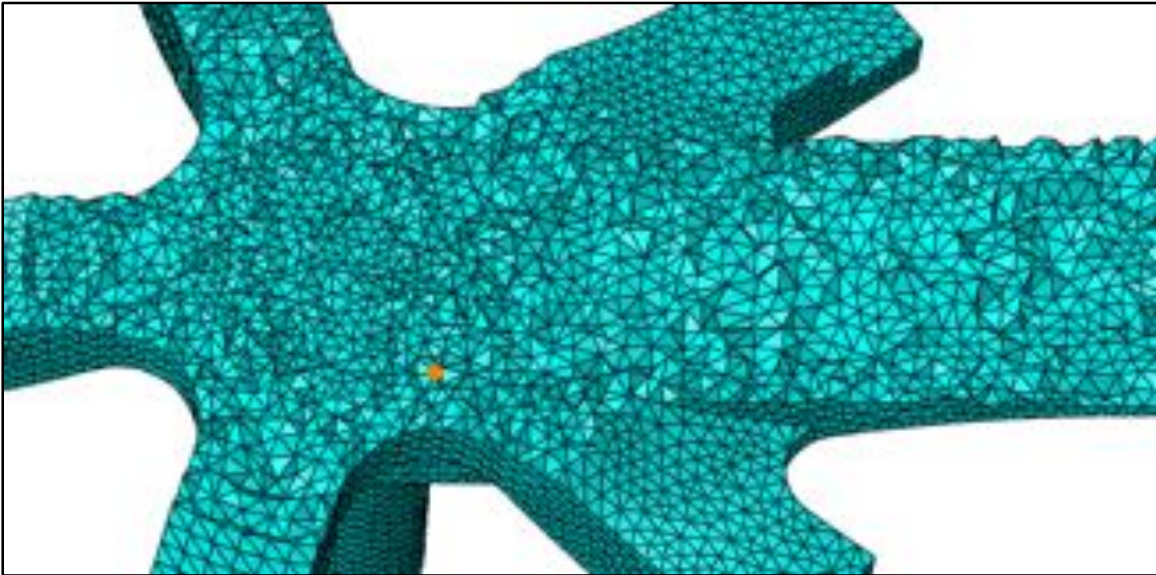


Figure 32: Horizontal Cut for Crank Mesh

Section 4: Development and Description of the Model Assembly and Boundary Conditions

Given below are the loading conditions and material properties that were used in the development of the finite element model.

Frame

According to [8], Al 6061-T6 is the most common material for bicycle frames. The material properties for this Al 6061-T6 are given in Table 1.

Table 1: Material Properties for 6061-T6 [9]

Elastic Modulus	68.9 GPa
Poisson's Ratio	0.33
Density	2700 kg/m ³
Shear Modulus	26 GPa

Zhongxia et. al. report that a rider exerts an average force of 235 N on the seat, 330 N on the handles, and 373 N on the pedal axle connection [10]. These will be modeled as pressure loads because they are simulating contact loads. In order to properly constrain the system, the connections to the rear wheel axle and front post will be fixed for all translations. This is all shown in Figure 33.

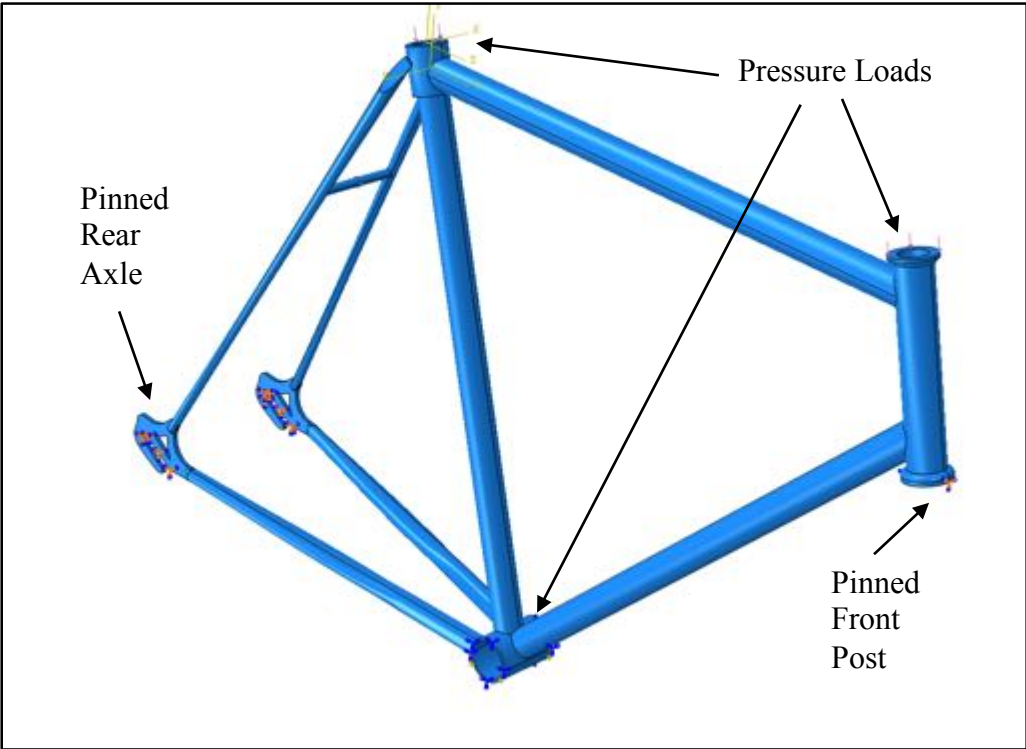


Figure 33: Frame Boundary Conditions and Loads

Crank Arm

Although more expensive bicycles have titanium or carbon fiber cranksets, most use Al 7075-T6 because it is cheap, light, and durable. Typical material properties for Al 7075-T6 are listed in Table 2.

Table 2: Material Properties for Al 7075-T6 [9]

Elastic Modulus	71.7 GPa
Poisson's Ratio	0.33
Density	2810 kg/m ³
Shear Modulus	26.9 GPa

According to Kautz and Hull [11], the maximum force applied to the pedal occurs when the crank is at 90° (i.e. half-way between the top and bottom of the stroke). At 90 rpm, the maximum vertical force is 300 N (down). The vertical force is represented by a uniform pressure on the inside surface of the hole. The constraint of the chain can be simulated by fixing the position of the spokes. The loading conditions are shown in Figure 34.

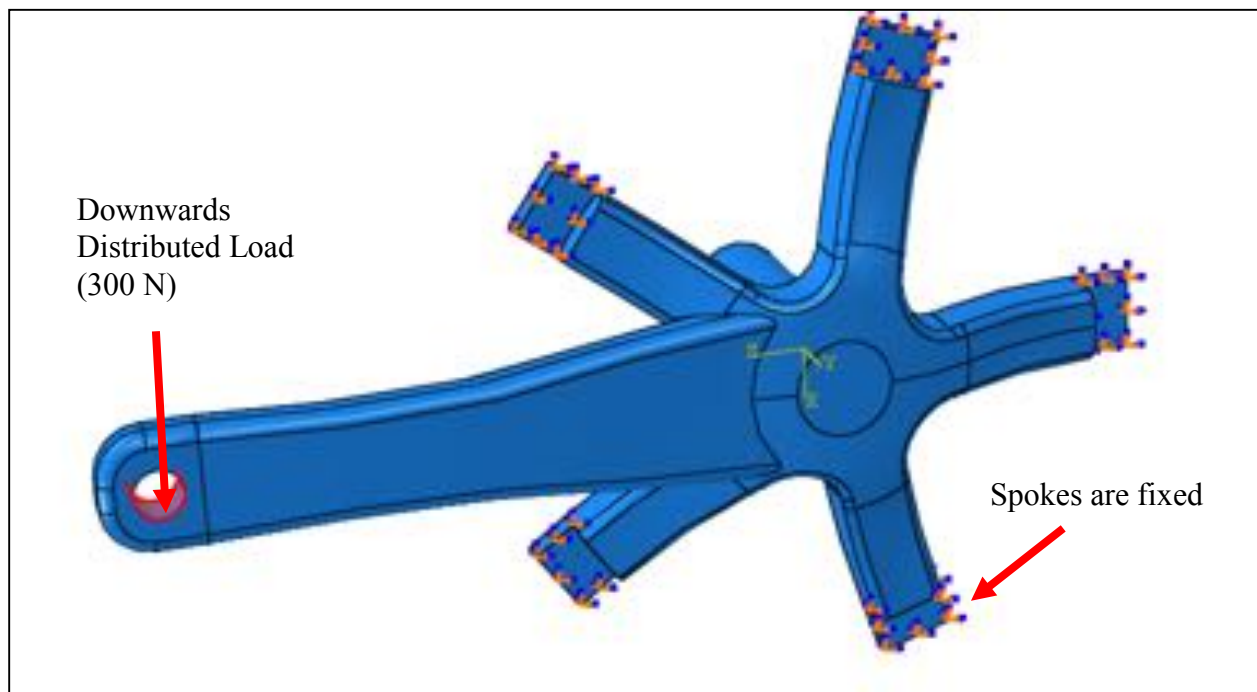


Figure 34: Loading Conditions of Crank Arm

The loading conditions shown in Figure 34 were obtained by first setting the displacement for the ends of each spoke to zero. Next, a downwards pressure load equivalent to 300 N was applied to the bottom half of the inside of the hole. This pressure simulates the contact load from the pedal's connector pin.

Gear

Like the crank arm, Al 7075-T6, whose properties listed in Table 2, was used as the material for the gear. For boundary conditions, the teeth in contact with the chain were pinned to simulate resistance from the chain. This is shown in and Figure 35.

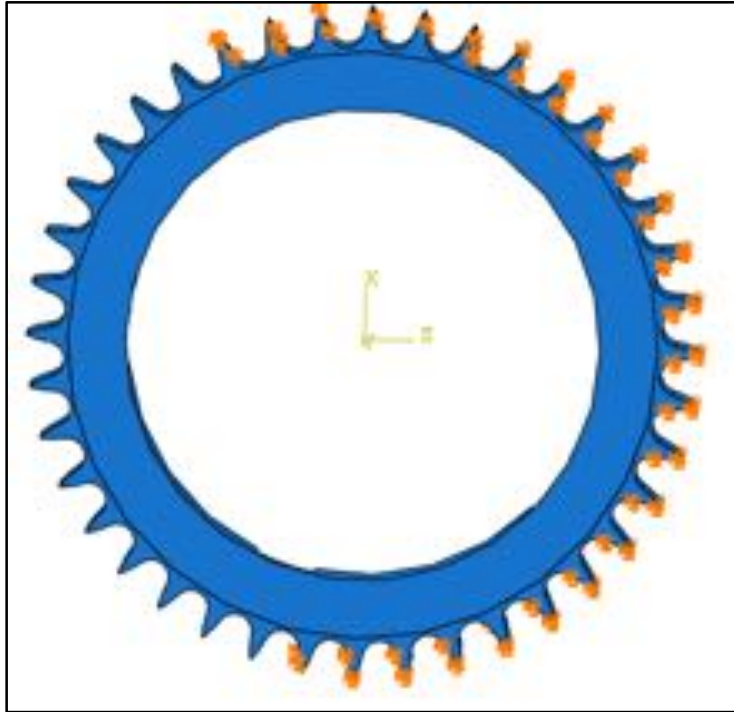


Figure 35: Pinned Teeth on Gear

To simulate the force applied by the crank, pressure forces will be assigned to the connecting surfaces. These forces were set equal to the reaction forces from the crank simulation. This came to about 410 N on the groove opposite the crank arm, 120 N on the two grooves surrounding that one, and negligible forces on the remaining two. Figure 36 shows how the load was applied.

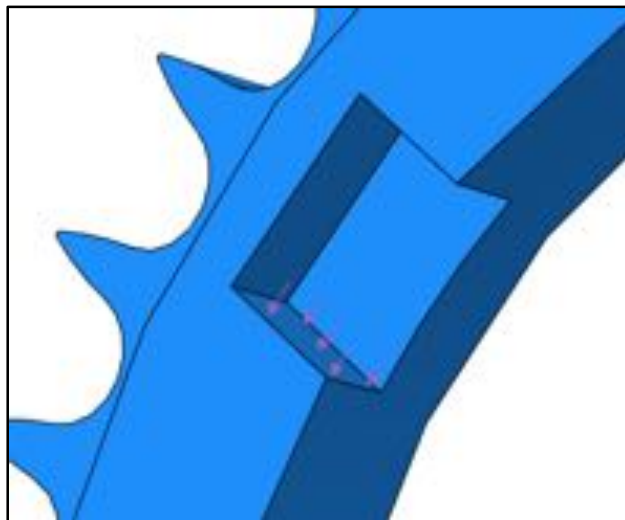


Figure 36: Pressure Load on Gear

Pedal

Bicycle pedals can be manufactured and purchased in many different materials. For this project, we chose a pedal with the same material as the bicycle frame and crank arm, which was Al 7075-T6. Typical material properties are listed in Table 2.

After creating the pedal in Abaqus, boundary conditions needed to be applied. According to Kautz and Hull [11], the maximum force exerted on a pedal occurs when a pedal is at the 90° (horizontal) from the top position of the pedal cycle. As the first boundary condition, the pin connection that holds the pedal to the crank was given a fixed condition in all directions. This is shown in Figure 37.

To simulate the force of the cyclist pushing down on the pedal, a uniform pressure load totaling 300 N was applied to the top surface of the pedal in the negative y-direction (downward). This is shown in Figure 38.

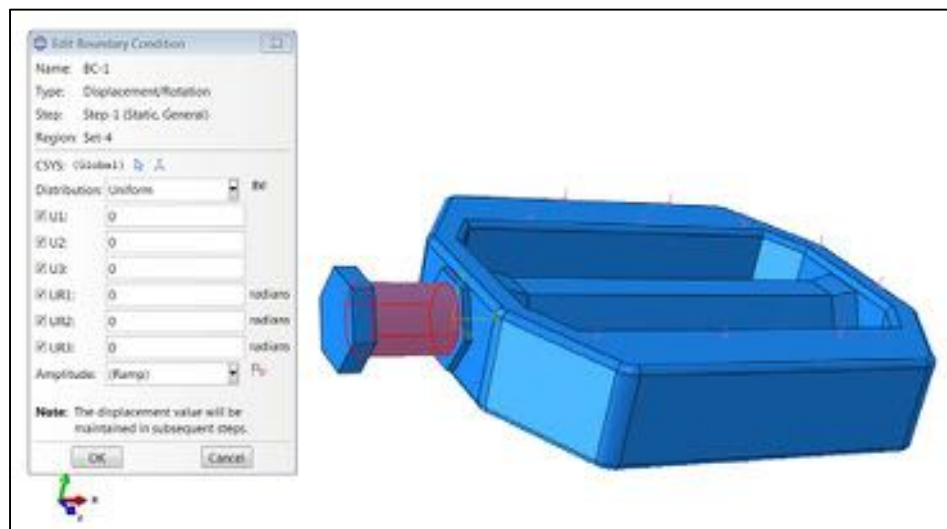


Figure 37: Selecting Boundary Condition Surfaces and Conditions

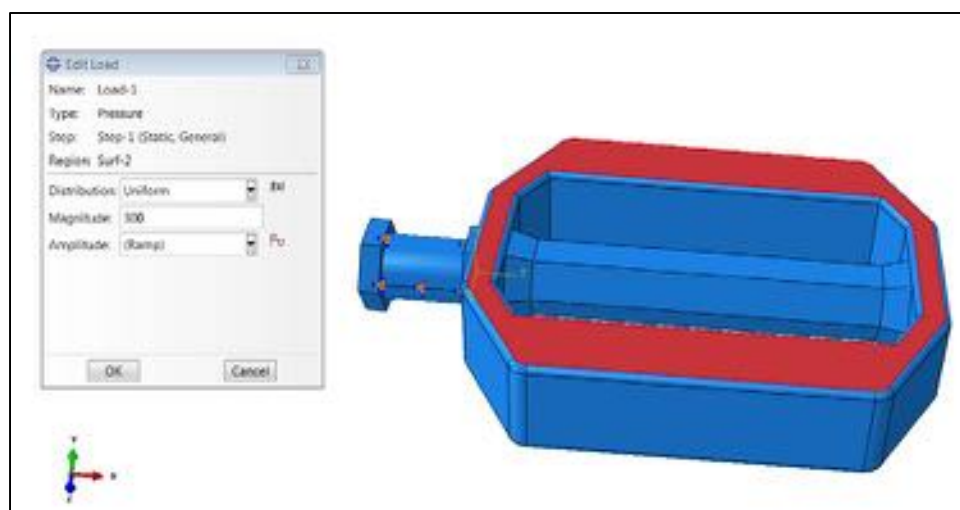


Figure 38: Choosing the Pedal's Loaded Surface and Magnitude of the Load

Section 5: Analysis of Finite Element Model

All models were run using Abaqus 6.13-2 in parallel on 16 CPUs. All steps were general static and the step size was 1 second.

Frame

The stress distribution for the frame is shown in Figure 39. As stated in the figure, the maximum calculated von Mises stress for the frame was 35.67 MPa. Since the yield strength of Al 6061-T6 is approximately 276 MPa, this is well within limit [9].



Figure 39: Frame Stress

Figure 40 shows a close-up of the stress distribution around the area where the pedal axle passes through the frame. As expected, the sharp transition in geometry that is produced where the tubes meet causes higher stresses.

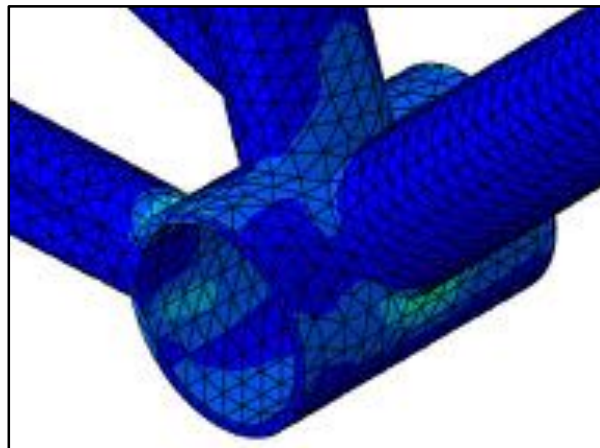


Figure 40: Frame Stress Close-up

Figure 41 shows the displacement for the frame. As the figure shows, the maximum displacement was 72.63 μm. As one would expect, the largest displacements occurred at the thinnest sections (located near the rear axle connection).

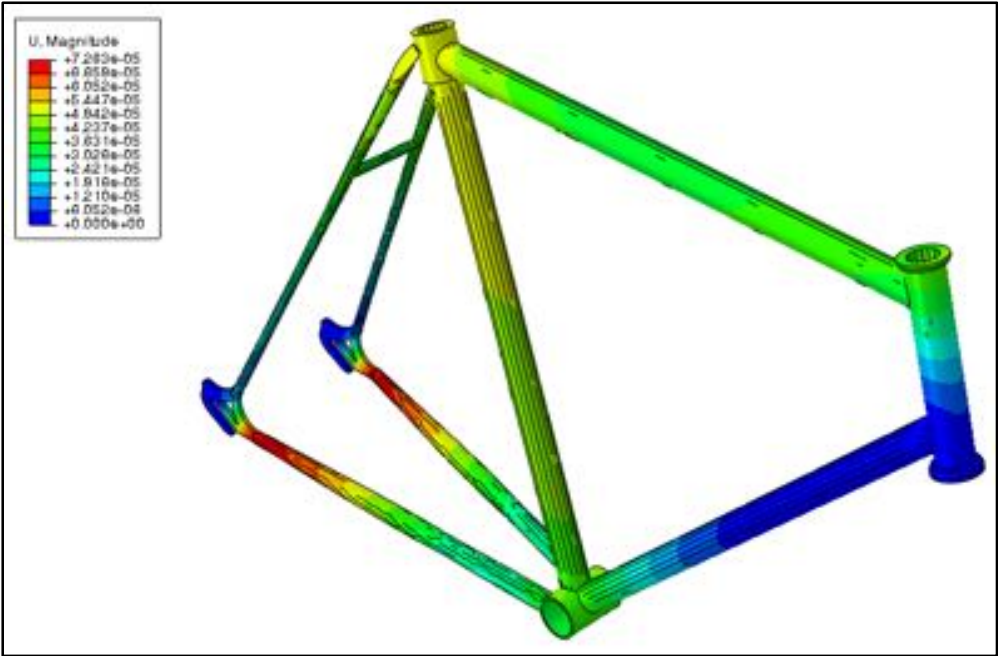


Figure 41: Frame Displacement

Figure 42 shows the strain for the frame. The maximum was 4.629×10^{-4} m/m, and the highest strains occurred near the rear axle connection. This is because that area is particularly thin and is the location of a fixed boundary condition.

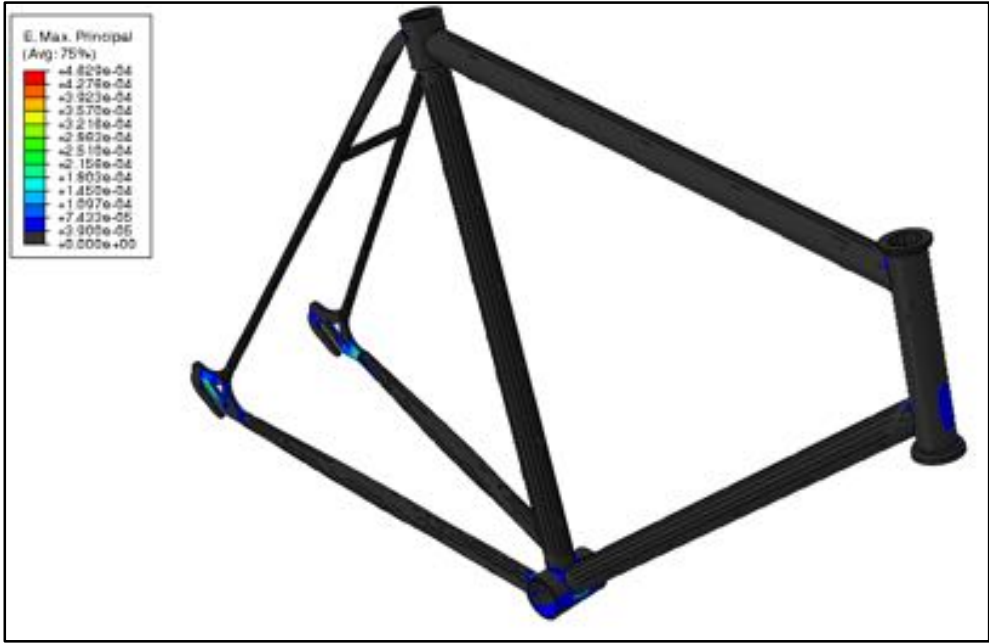


Figure 42: Frame Strain

Figure 43 shows the von Mises stress and maximum principle strain for an element near the rear axle. This element was chosen because it is located in area with high stresses, so it will likely be among the first to fail. Since the simulation was conducted using static analysis, the values grow linearly with time.

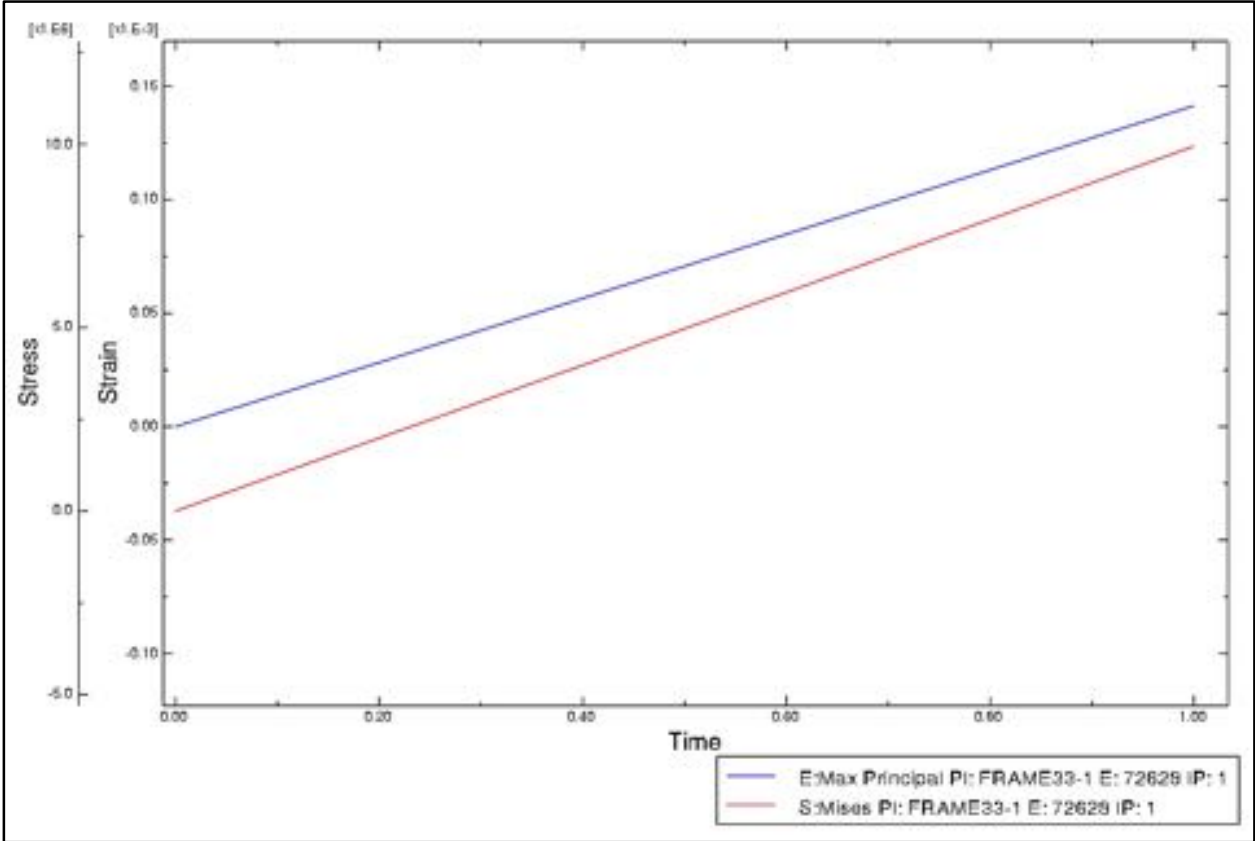


Figure 43: Stress and Strain for Frame Element near Rear Axle

Gear

Figure 44 shows the stresses for the gear. Elements with a von Mises stress lower than 1.70×10^6 were excluded (shown as dark grey) in order to better highlight the high stress elements. The maximum von Mises stress was 21.55 MPa. Since the yield stress of Al 7075-T6 is approximately 503 MPa, this gives a large margin of safety [9].

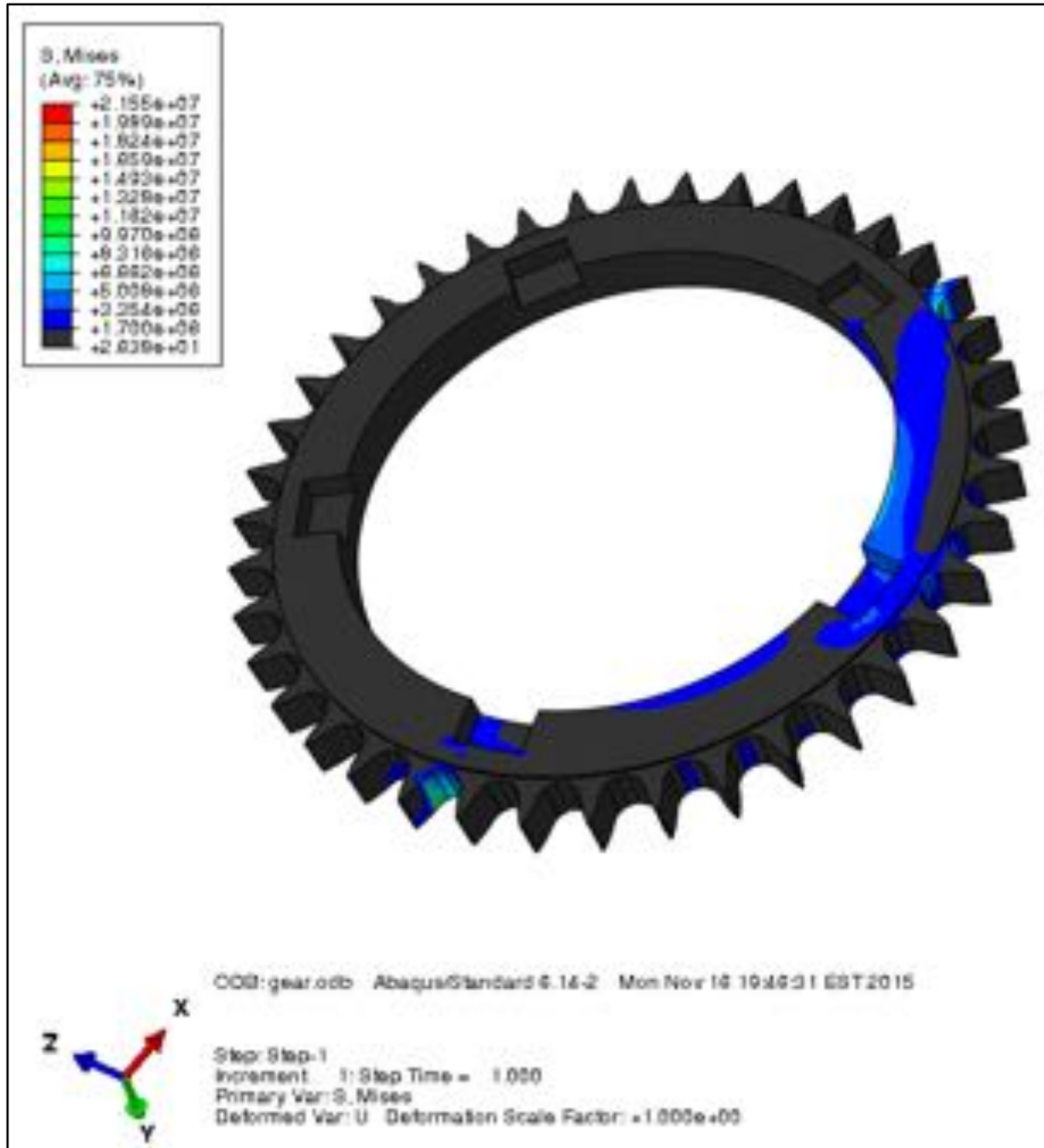


Figure 44: Gear Stress

The nodal displacements for the gear are shown in Figure 45. The maximum displacement was 9.036 μm. The displacements are concentrated on one side because the chain held the other side in place.

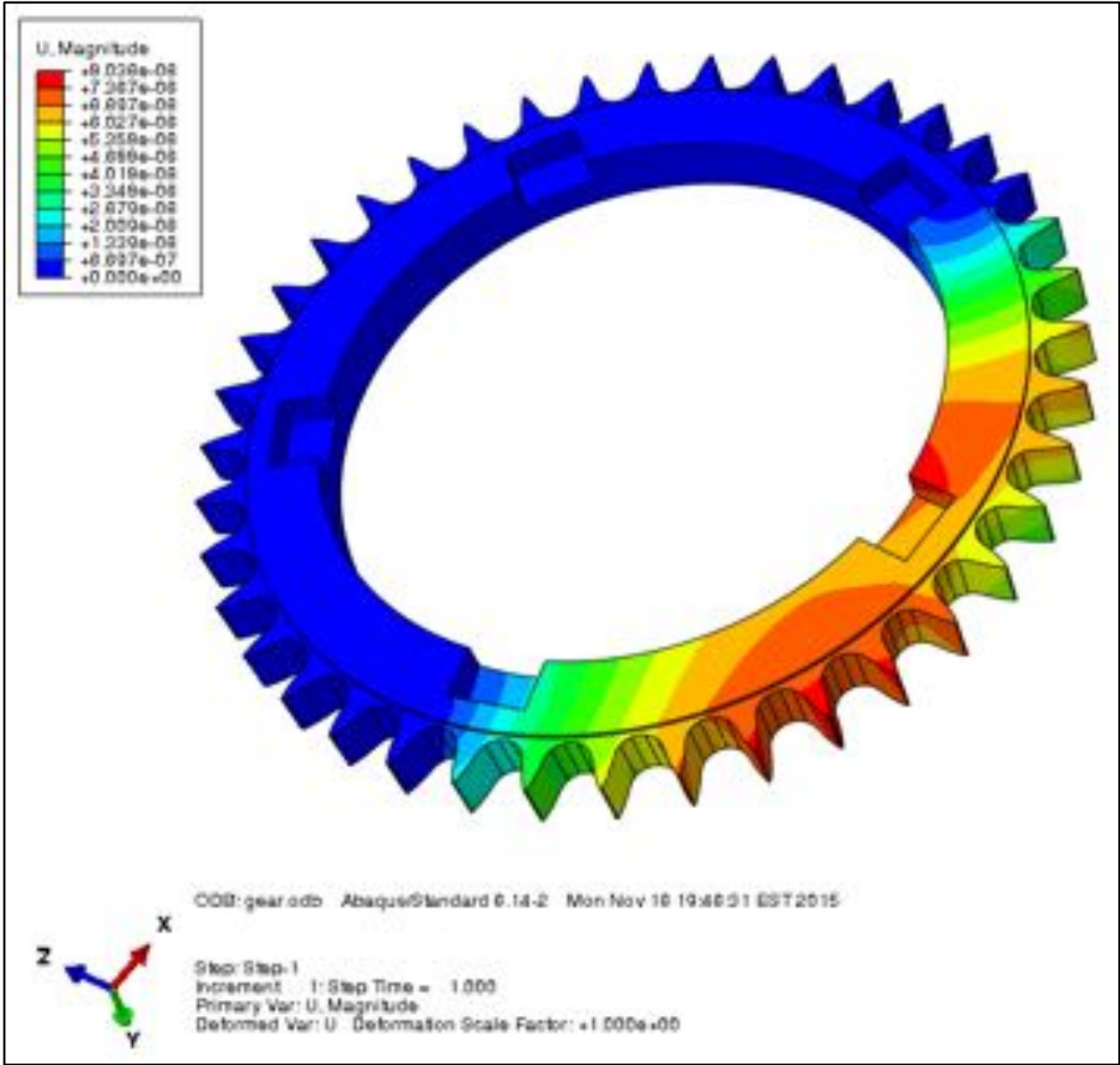


Figure 45: Gear Displacement

Figure 46 shows the strain for the gear. Like the stress picture, the low value elements were excluded (shown as dark gray) to highlight the high value elements. As the figure shows, the maximum strain was 3.101×10^{-4} m/m. Additionally, the figure illustrates the fact that the highest strain occurred where the highest load was applied.

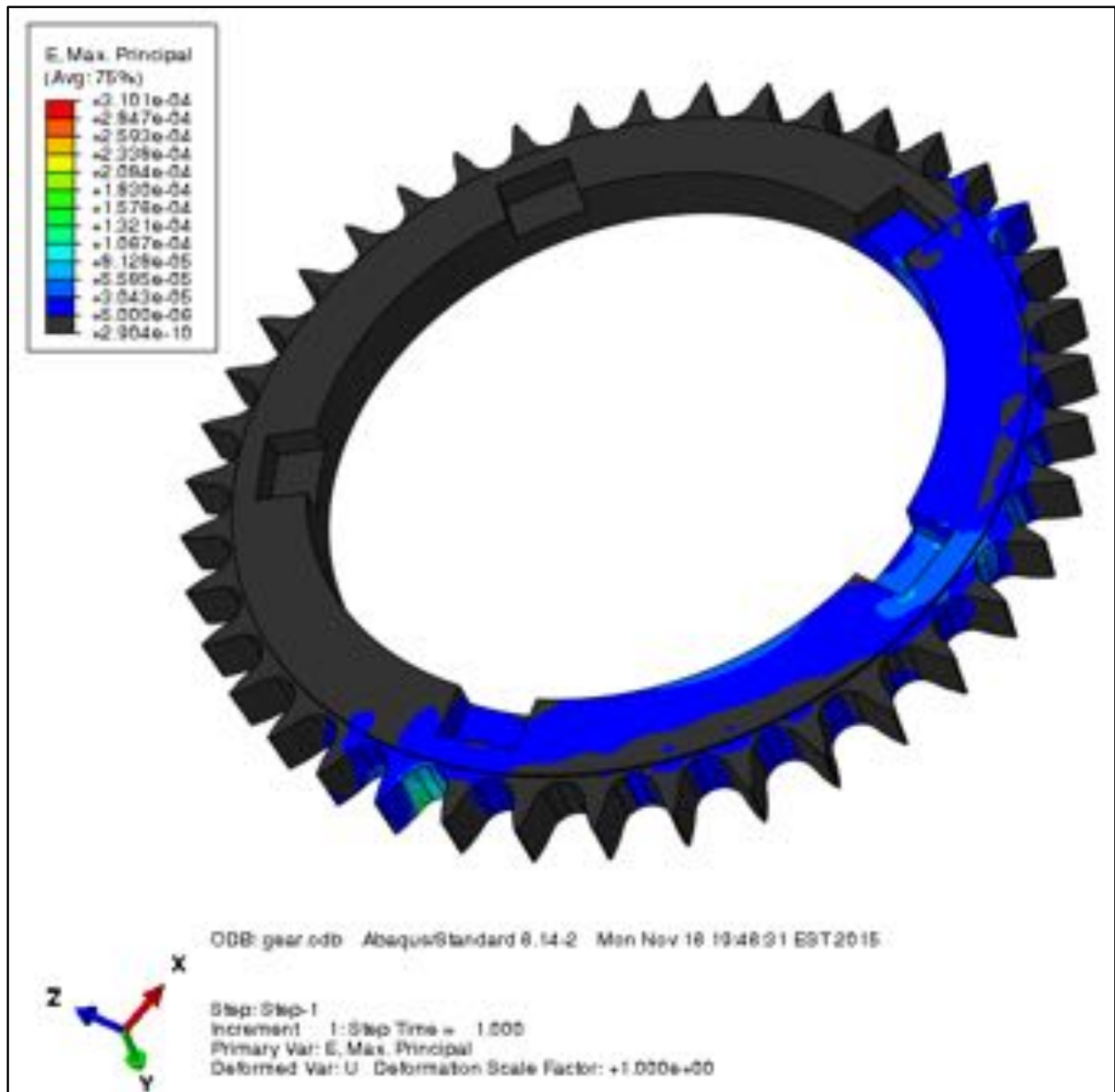


Figure 46: Gear Strain

Figure 47 shows the von Mises stress and maximum principle strain for an element near the base of a tooth. As with the plot for the frame, this element was chosen because it is located in area with high stresses, so it will likely be among the first to fail. Since the simulation was conducted using static analysis, the values grow linearly with time.

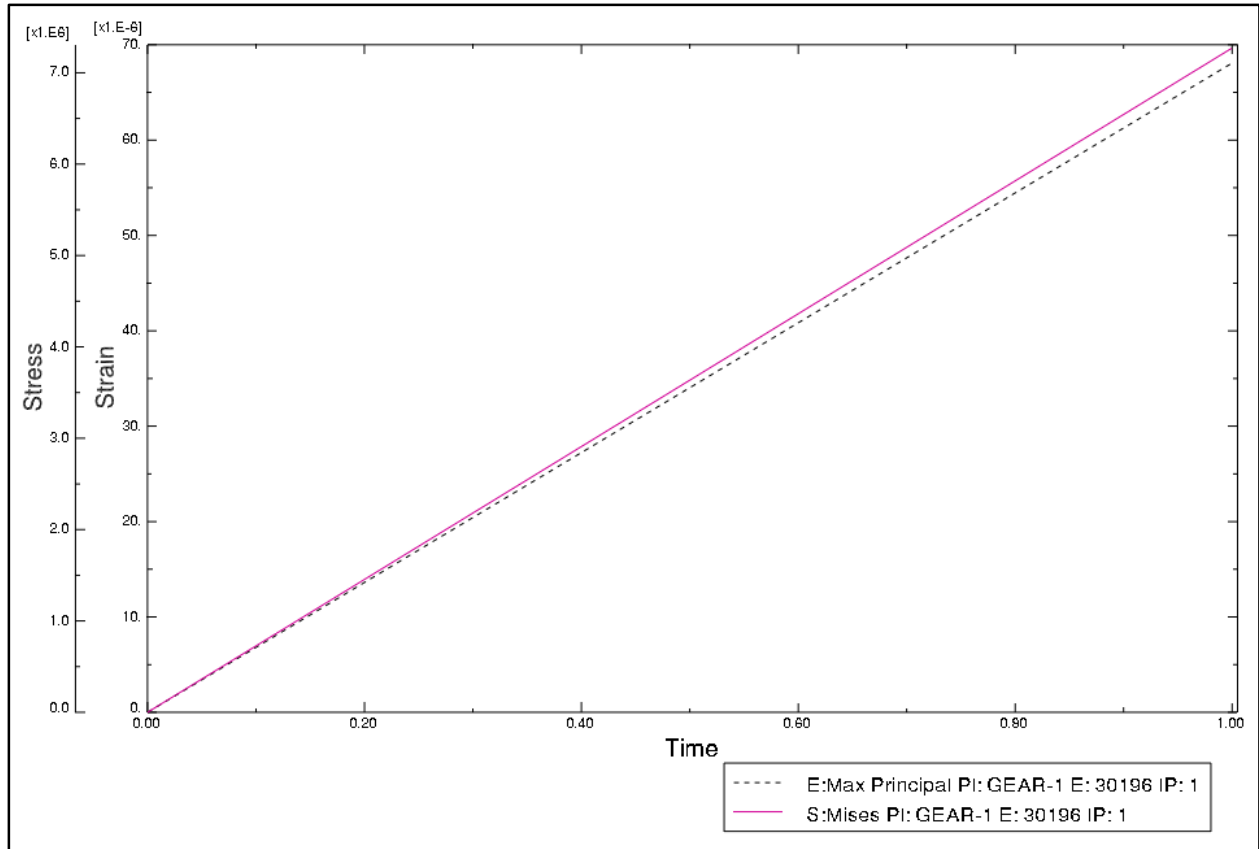


Figure 47: Stress and Strain for Volatile Gear Element

Crank

Using the pre-described boundary conditions and the 300 N distributed load pin hole, static analysis was conducted in Abaqus. The resulting stress contour is shown in Figure 48. The maximum stress was 14.19 MPa, which is far below the yield stress of 503 MPa.

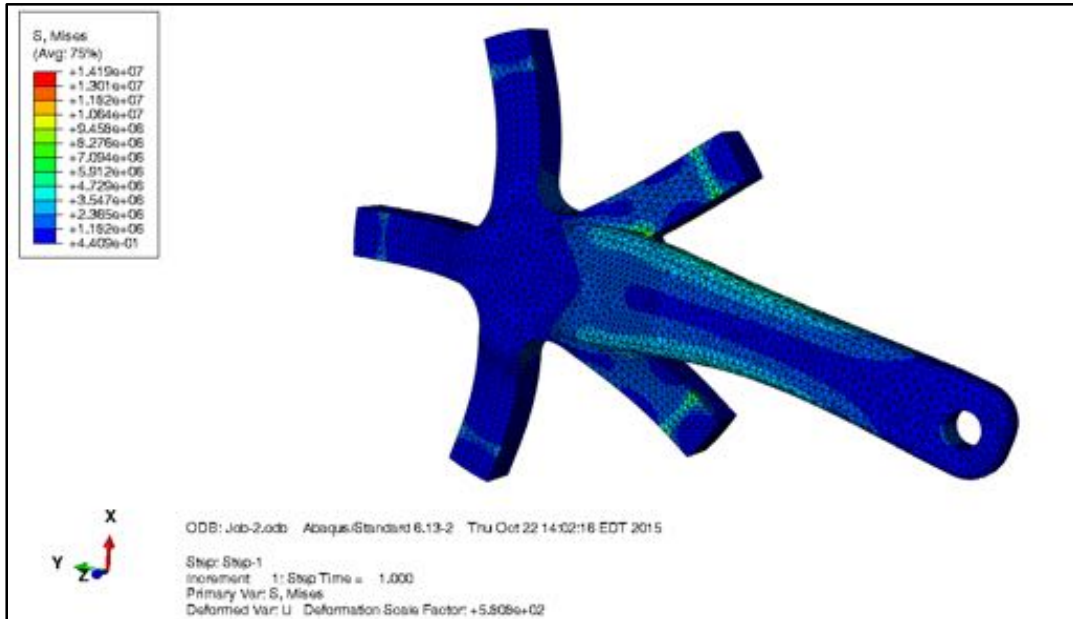


Figure 48: Stress Contour of the Crank

The stress contours that were found are a result of the boundary conditions and geometry. Since the main arm is longer and thinner than the central structure, it experienced higher stresses than most areas. Furthermore, the highest stressed elements can be found where the arm meets the spokes. This is a result of the major geometric discontinuities at that location. Figure 49 shows a cut plane view of the crank arm at these high stress elements.

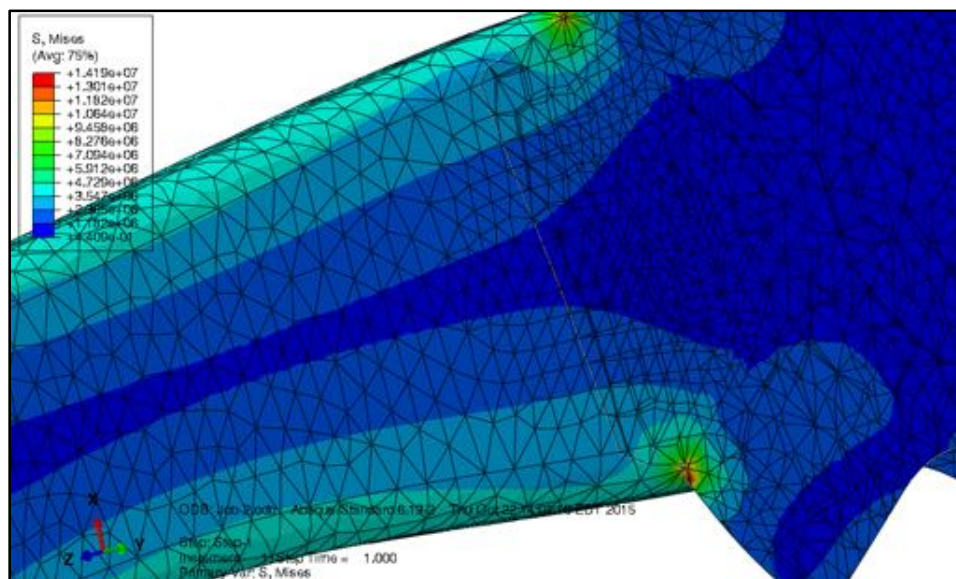


Figure 49: Crank's Most Stressed Elements Cut Plane View

Figure 50 shows the strain contour for the crank. The maximum strain was 2.024×10^{-4} m/m. Most of the high strain regions are at the base of the main arm because this configuration is somewhat analogous to a cantilevered beam. Again, the geometric discontinuity where the main arm meets the central body created high values, which can be seen in Figure 51.

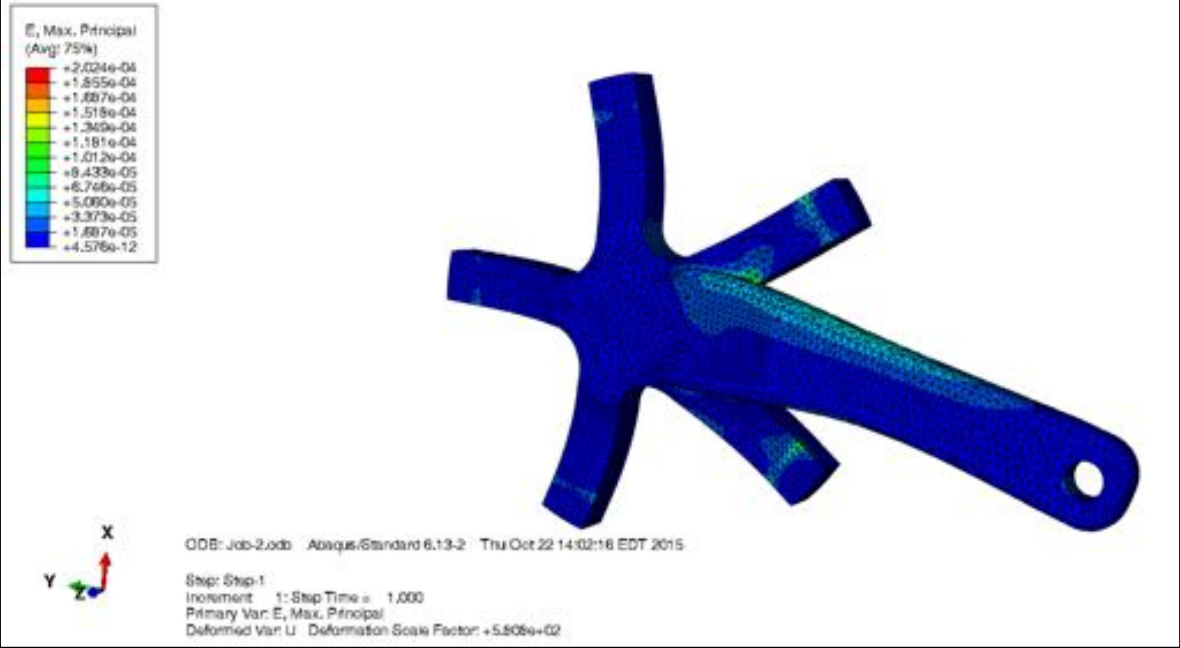


Figure 50: Strain Contour of the Crank

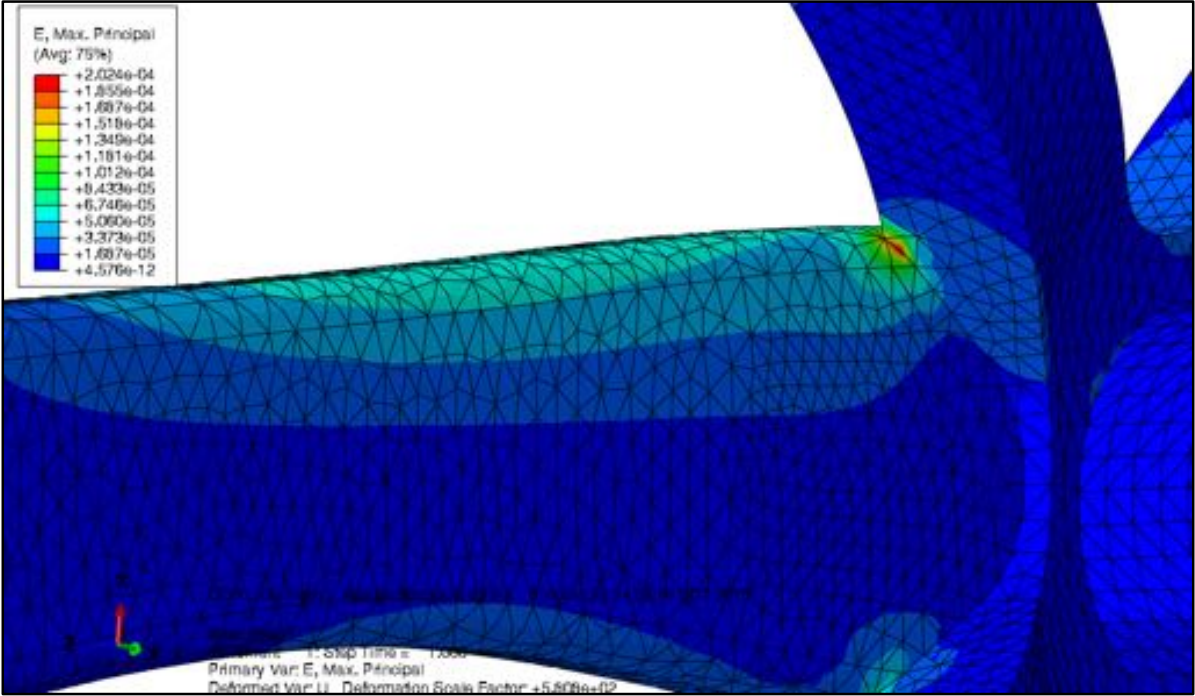


Figure 51: Close View of Most Strained Elements in Crank

In addition to analyzing the stress with respect to time, our team also considered the stress evolution as a function space. Figure 54 shows the path that was selected for analysis, and Figure 55 shows the stress values at every point in that path. It is readily apparent that the stress grows as the path approaches the point where the crank arm joins with the crank body. This is to be expected since the crank arm acts like a cantilevered beam. At the very end, the stress decreases slightly as the evaluation points have passed into the thicker section of the crank body.

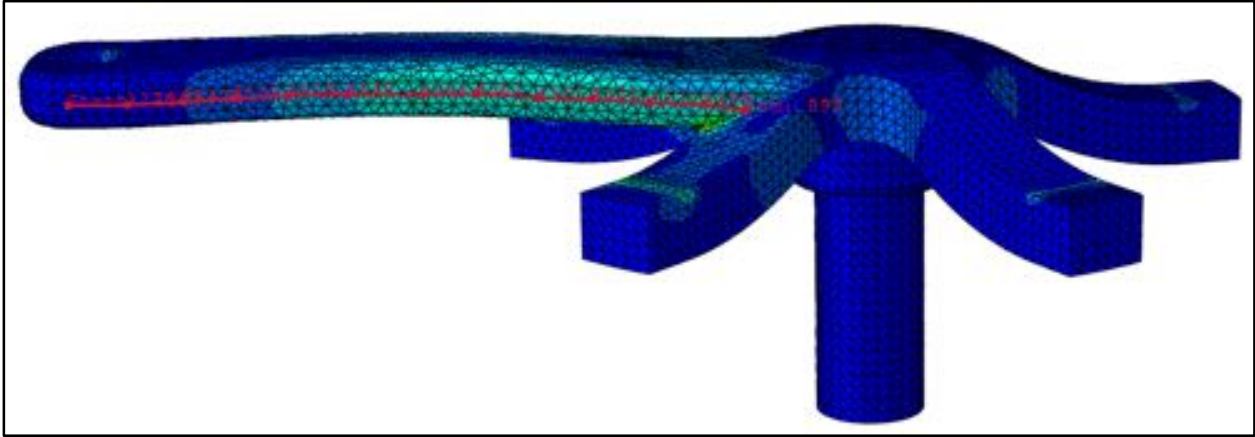


Figure 54: Crank Path

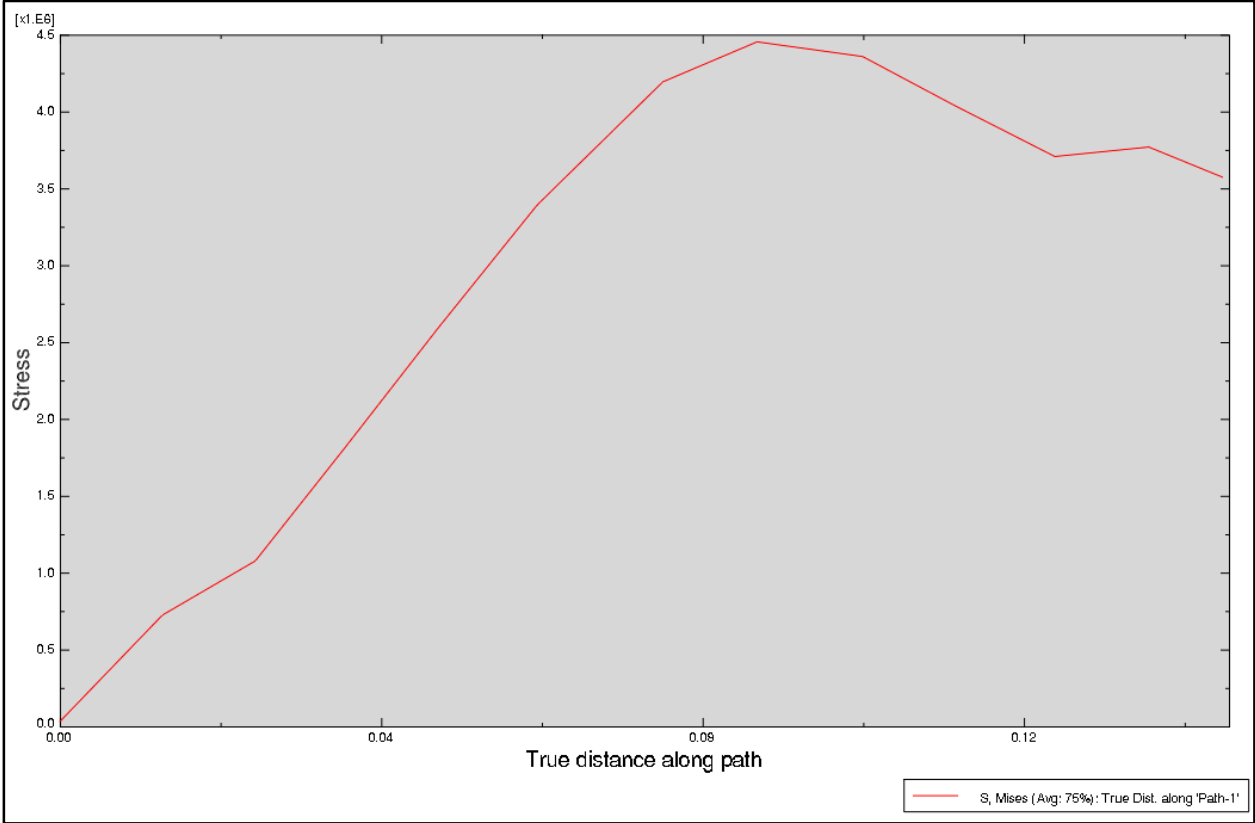


Figure 55: Stress Values for Crank Path

Pedal

Using the boundary conditions that have been previously described and the 300 N distributed load on the top surface of the pedal, a static simulation was conducted on the pedal in Abaqus. The resulting stress contour can be found in Figure 54. Figure 55 shows a close up of the most stressed elements in the mesh. The maximum stress was 123.6 MPa.

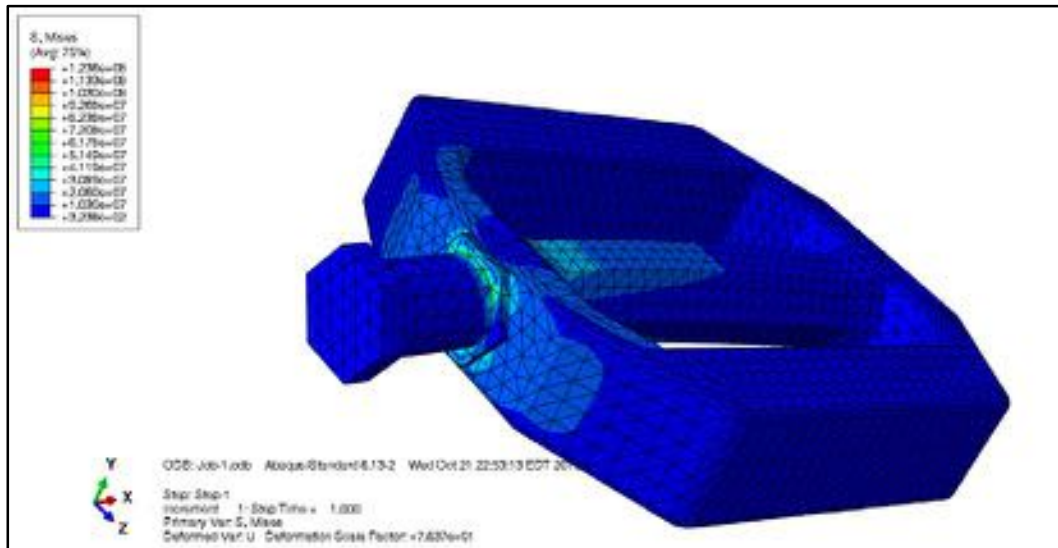


Figure 56: Stress Contour of Entire Pedal

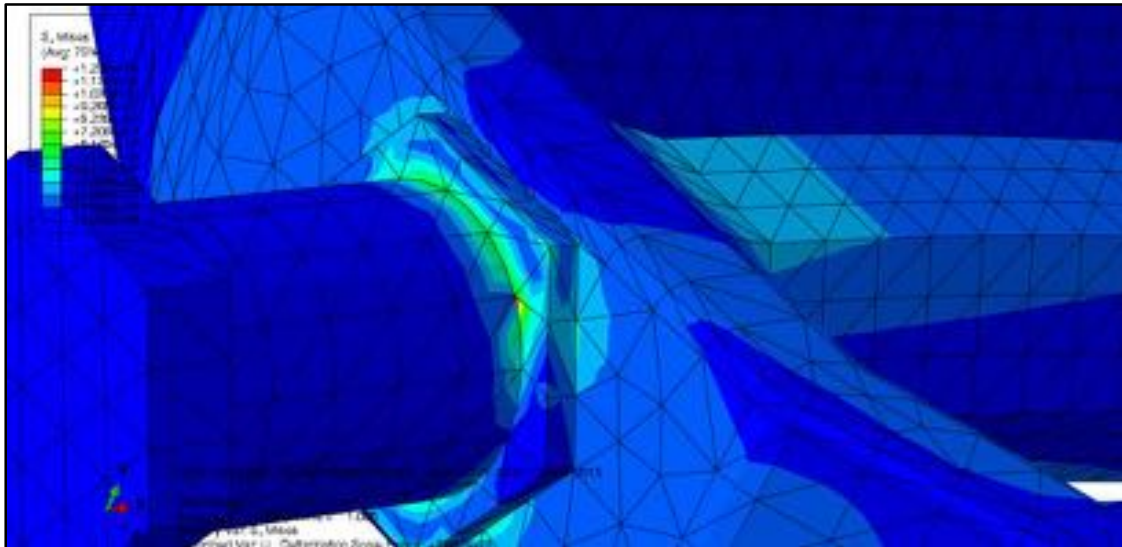


Figure 57: Close View of Most Stressed Elements in the Pedal

The high stresses at the base of the pin are a result of both geometry and loading conditions. In terms of geometry, this area represents a major discontinuity as the model transitions from the pedal to the pin. The loading condition, which fixed the pin, effectively made this area a fulcrum for the distributed load, so the bending stresses were concentrated here.

In addition to stress contours, strain and displacement contours were generated. Figure 56 shows the strain contour for the pedal and Figure 57 shows the displacement contour for the pedal. The deformation contour is exaggerated by a scale factor of 7.637. The maximum strain was 2.010×10^{-3} m/m and the maximum displacement was 144.3 μm .

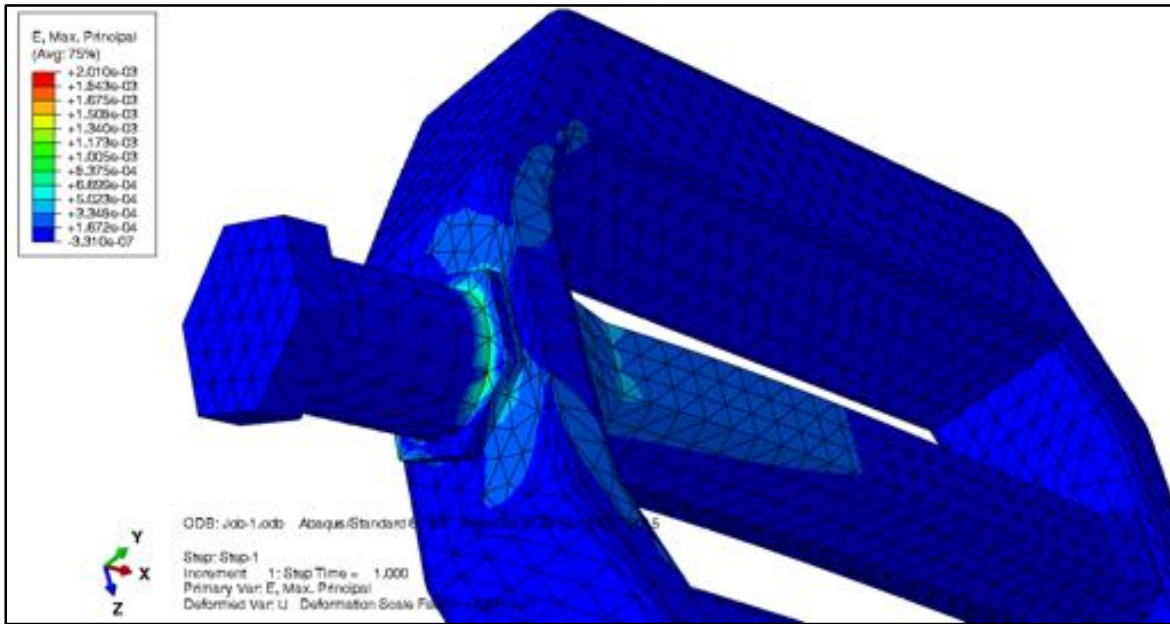


Figure 58: Strain Contour of the Pedal

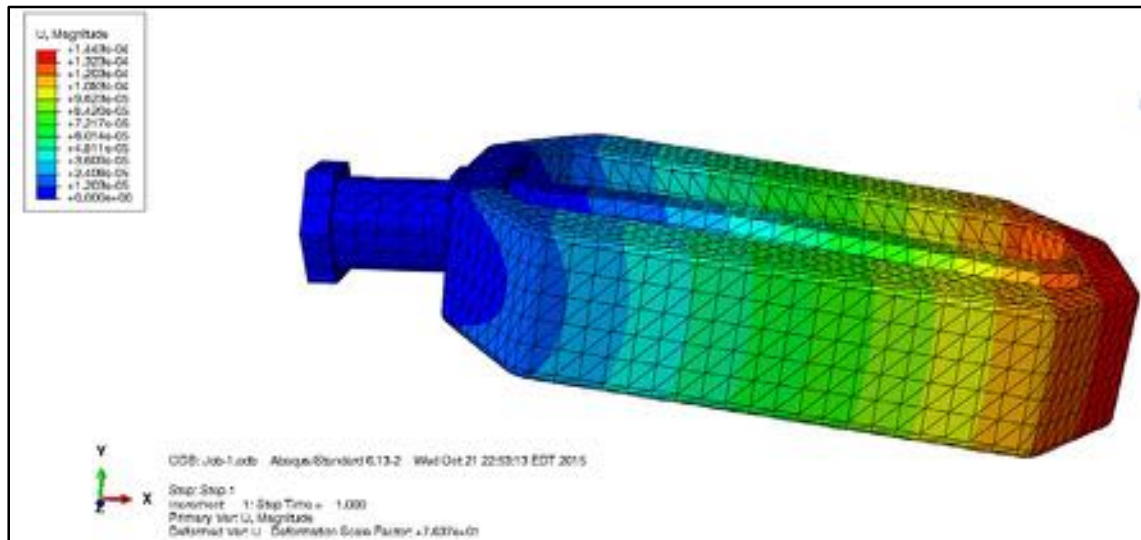


Figure 59: Deformation Contour of the Pedal

Figure 58 shows the von Mises stress and maximum principle strain for an element near the connection between the footpad and the axle. As with the plot for the crank, this element was chosen because it is located in area with high stresses, so it will likely be among the first to fail. Since the simulation was conducted using static analysis, the values grow linearly with time.

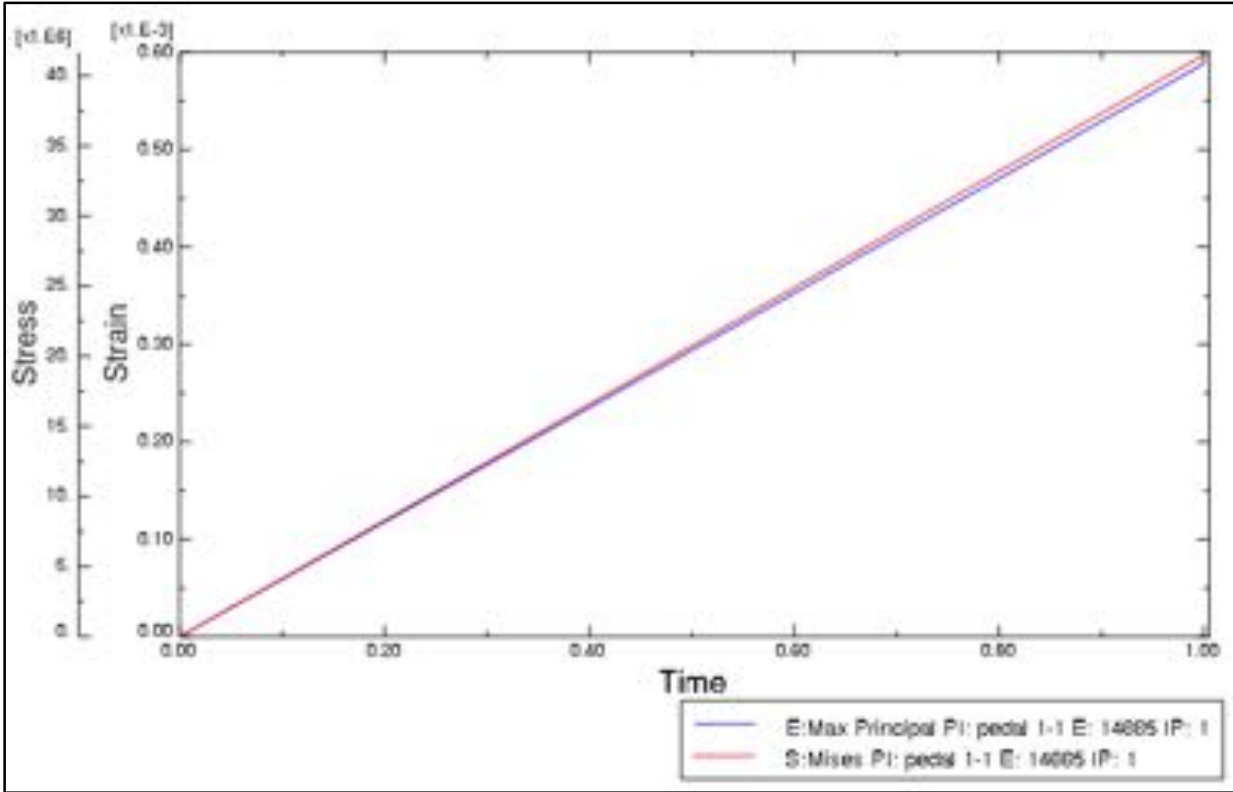


Figure 60: Stress and Strain Plot for Pedal

As with the crank, the stress was also analyzed with respect to position. Figure 61 shows the path that was considered. Figure 62 shows the stress value at each of the elements along that path. As Figure 62, the pedal acts much like a cantilevered beam, with the stresses decreasing in proportion to the distance from the fixed area. The high spike in stress that can be observed around distance 0.02 is due to the stress concentration at the intersection between the pin and the foot area.

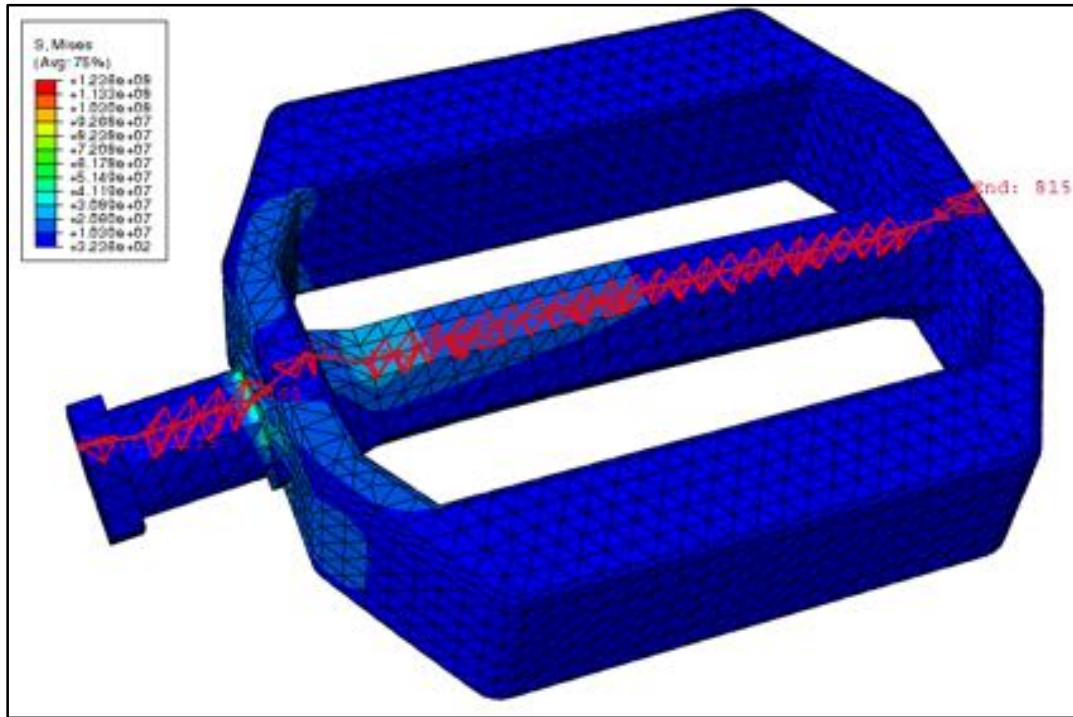


Figure 61: Pedal Path

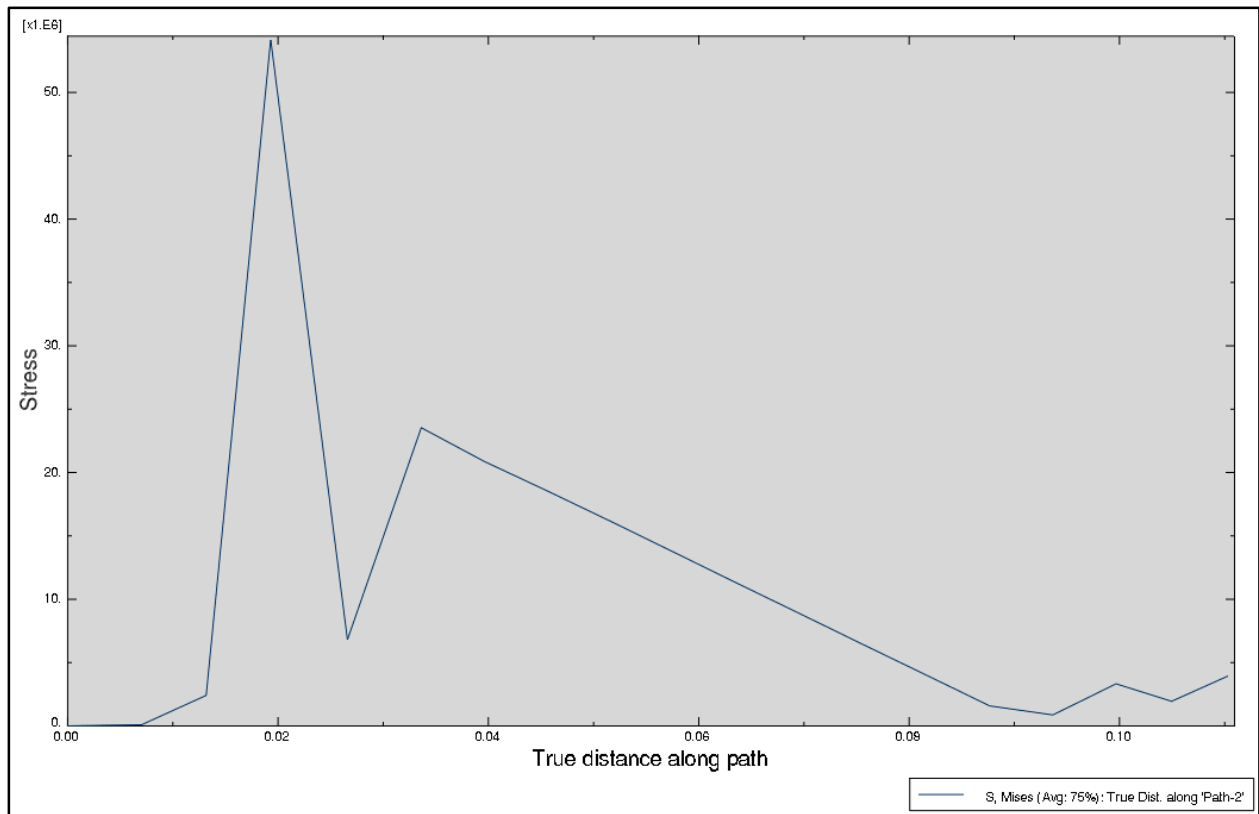


Figure 62: Pedal Path Stress Plot

Section 6: Additional Analysis of Frame

Since the frame is arguably the most important component of the bicycle from a structural analysis viewpoint, our team conducted additional analysis on it. This includes modal analysis and dynamic analysis. In order to complete these more advanced analyses, a stronger geometry was procured from an open-source online repository [12]. The geometry is shown below in Figure 61. The same materials and meshing techniques described above were used to prepare this model.



Figure 63: New Frame Geometry

Modal Analysis

To conduct the modal analysis of the frame, fixed boundary conditions were applied where the frame contacts the rear axle and the front fork, as shown in Figure 62. Abaqus CAE was then used to perform a frequency analysis using a linear perturbation step. Three eigenvalues were queried, and the results are shown in Table 3. These values correlate with those observed experimentally for similar designs [13]. Visualization of these three modes are shown in Figure 63, Figure 64, and Figure 65, respectively.

Table 3: Natural Frequencies of Frame

Mode	Value	Frequency (Hz)
1	$1.039 \cdot 10^6$	162.21
2	$2.573 \cdot 10^6$	255.32
3	$4.836 \cdot 10^6$	349.98



Figure 64: Modal Boundary Conditions

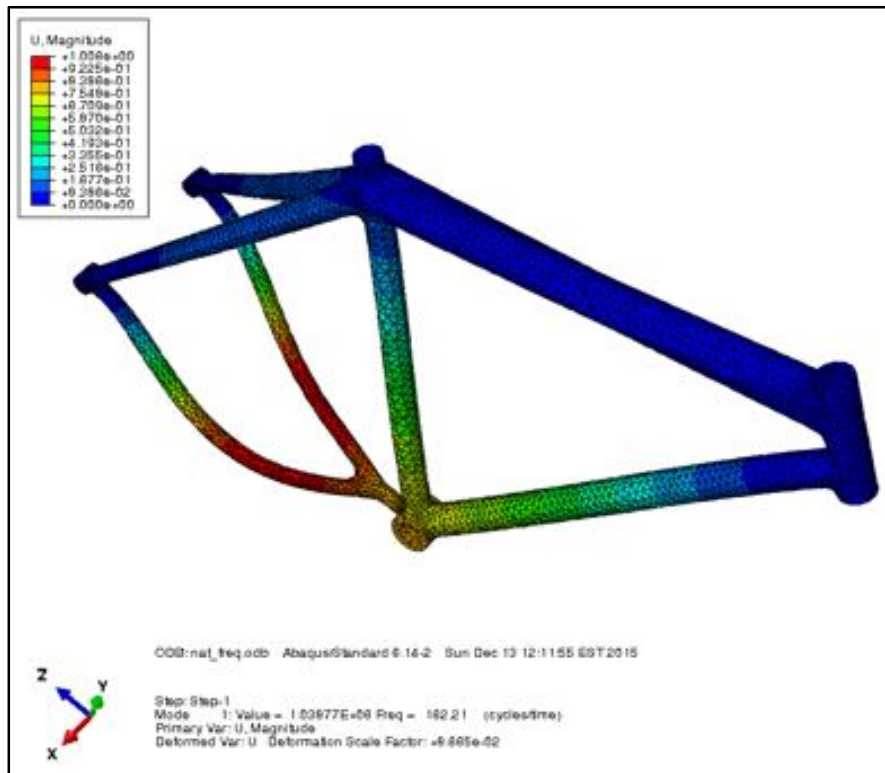


Figure 65: Mode 1 for Frame

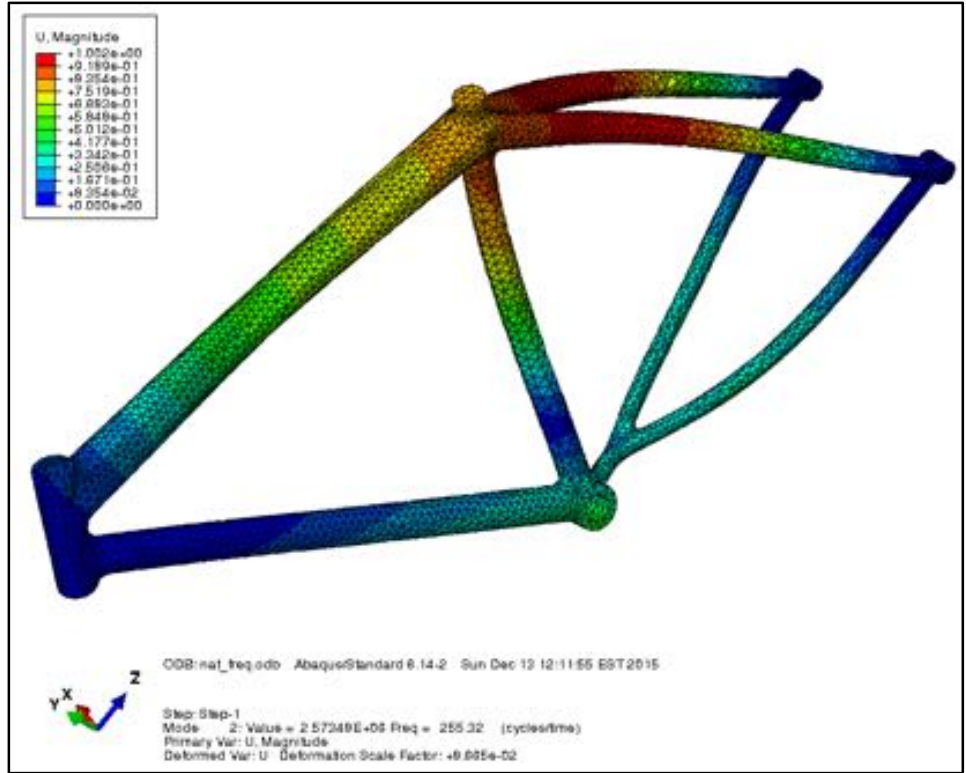


Figure 66: Mode 2 for Frame

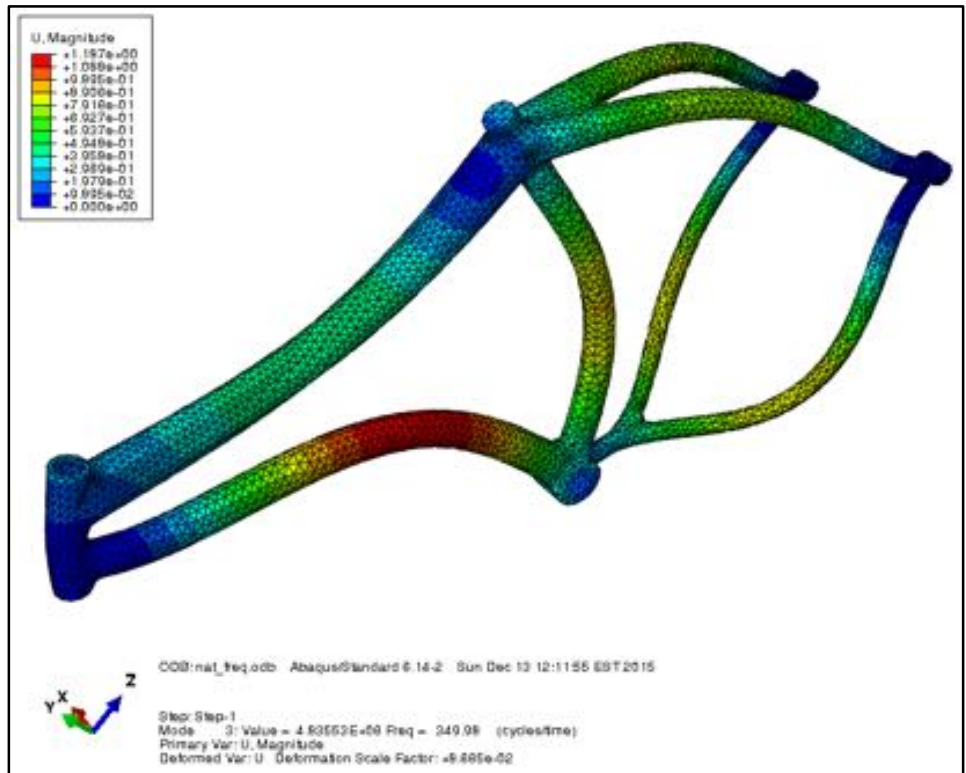


Figure 67: Mode 3 for Frame

Dynamic Analysis

Although static analysis is helpful in obtain benchmark values, a bicycle is obviously not a static machine. Therefore, our team conducted dynamic analysis evaluate the frame response induced by impacting the ground after a 1 meter jump. Using the fact that the bicycles vertical velocity must be zero when the maximum height is reached and Equation 8-1, our team calculated an impact velocity of approximately 4.4 m/s.

$$v_f^2 = v_0^2 + 2ax \quad (8-3)$$

According to Levy and Smith, the shocks and tires of an average bicycle absorb between 40% and 60% of the impact energy [13]. Therefore, our analysis employs an impact velocity of 2.2 m/s. To simplify the simulation, the front fork was given an upwards velocity instead of giving the frame a downwards velocity, as shown in Figure 70. The simulation was run for 1 ms, and a visualization of the stresses are shown in Figure 71. As Figure 71 shows, the stresses have already propagated across the entire frame after 1 ms. The maximum stress was 75.67 MPa, which gives a factor of safety of approximately 3.6 since the yield stress of Al 6061-T6 is about 275 MPa [9].



Figure 68: Initial Conditions for Impact

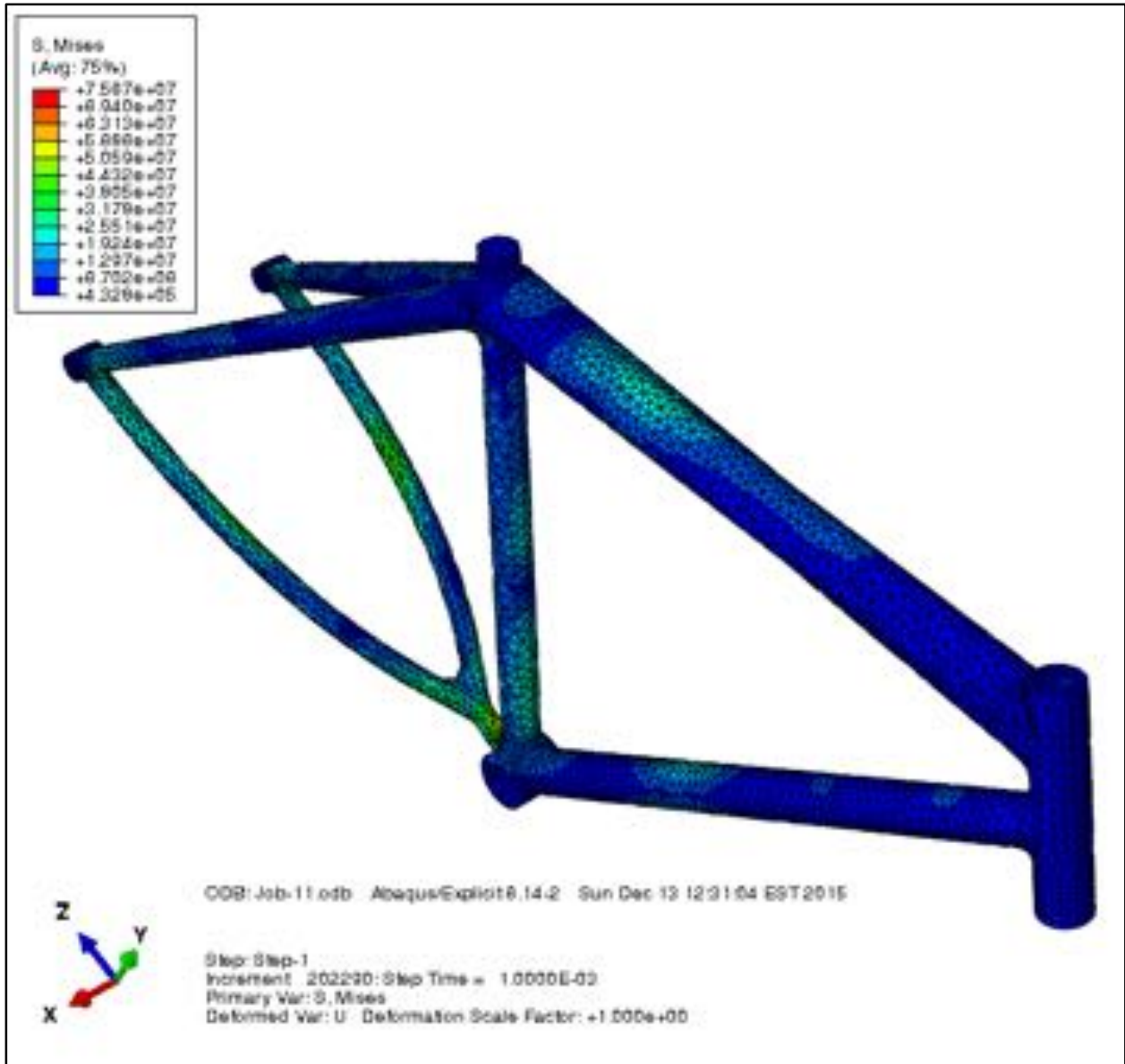


Figure 69: Impact Stress Contour at $t = 1 \text{ ms}$

Section 7: Summary of Major Findings

The purpose of this report was to develop design suggestions using the analysis described above. After a review of the simulations, our team determined three major conclusions concerning the design. The first is that variations in the tube sizes for the frame reduce structural efficiency. Figure 39 shows that almost all of the stresses induced in the frame are located in the thinnest tubes. This means that under normal loading conditions, these areas will fail first. As a result, the other, thicker tubes serve little purpose since once one tube fails, the bicycle is rendered effectively useless. Therefore, our suggestion is to either reduce the thickness of the thicker tubes to save on weight or increase the thickness of the thinner tubes to increase the effective structural integrity.

Our second design suggestion concerns the interface between the crank and gear. Currently, the connection between the gear slots and the crank spokes is a rectangular prism. All of those sharp angles act as stress concentrators, which induce large stresses in the gear (see Figure 44) and the crank spokes (see Figure 48). The stresses in the crank spokes are especially pronounced, as evidenced by the perpendicular stress lines near the spoke tips. Therefore, our suggestion is to round the interface, which should decrease the stress concentration. A possible design is shown below in Figure 59. The slot in the gear would be modified to fit this as well.

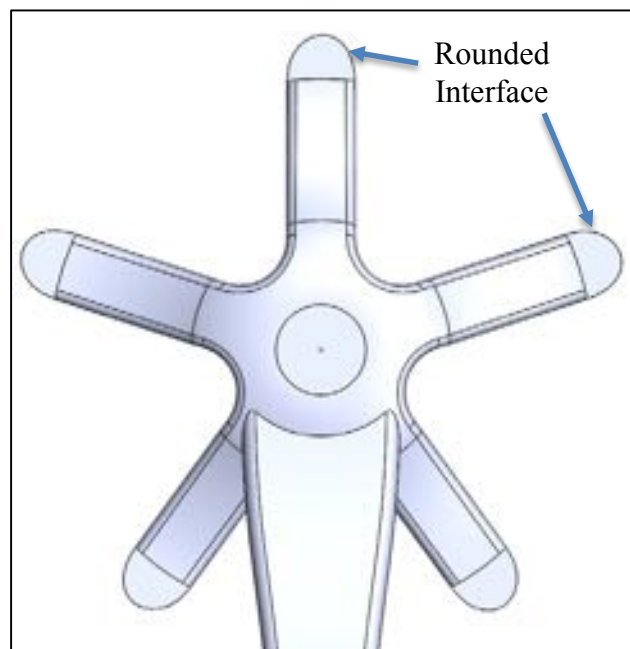


Figure 70: Alternative Design for Crank Spokes

The third and final design suggestion is for an integrated axle on the pedal. Figure 55 shows that most of the stresses in the pedal are concentrated on the edge between the pedal axle and the footpad. If the axle were integrated into the footpad, the transition could be made much smoother. As with the crank spokes, a smoother interface would reduce the stress concentration and improve durability. A possible design is shown in Figure 60.

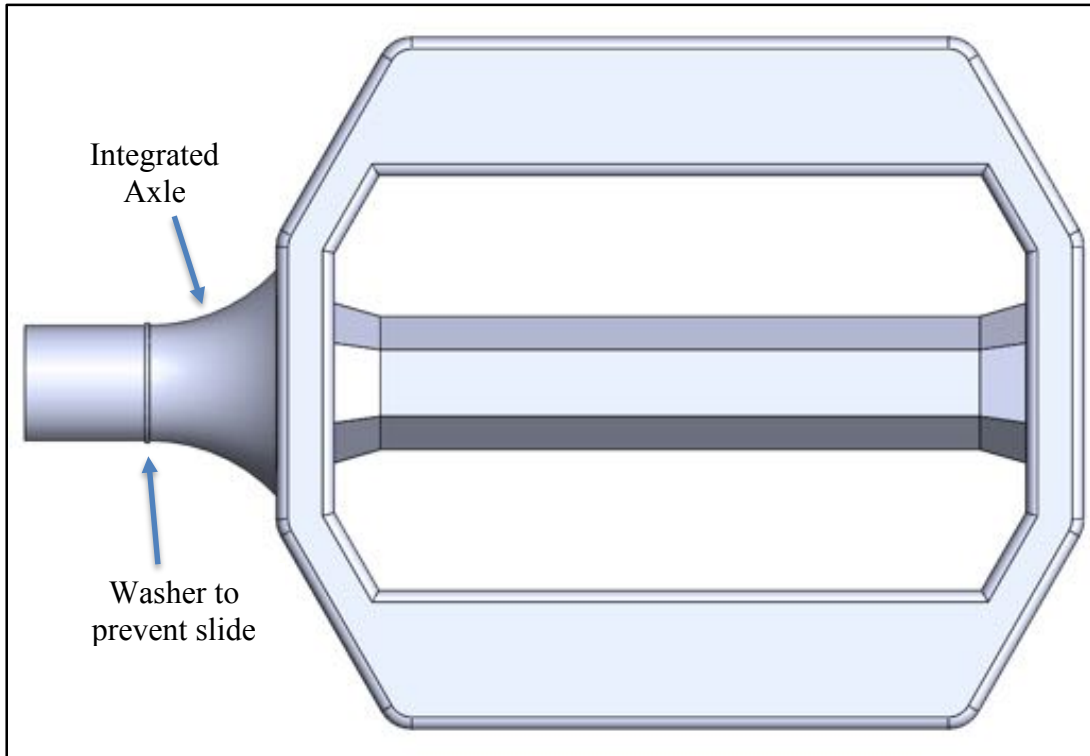


Figure 71: Alternative Design for Pedal

Section 8: Works Cited

- [1] "Number of cyclists/bike riders," Statista, [Online]. Available: <http://www.statista.com/statistics/227415/number-of-cyclists-and-bike-riders-usa/>. [Accessed 21 September 2015].
- [2] "Total population (in number of people)," World Bank, [Online]. Available: <http://data.worldbank.org/indicator/SP.POP.TOTL>. [Accessed 21 September 2015].
- [3] D. Arola, P. Reinhall, M. Jenkins and S. Iverson, "An Experimental Analysis of a Hybrid Bicycle Frame," *Techniques*, pp. 21-24, May/June 1999.
- [4] M. Pazare, "Stress Analysis of Bicycle Frame," *International Journal of Engineering Science and Technology*, vol. VI, no. 6, pp. 287-294, 2014.
- [5] D. Recker, "Concord Selecta 12 - Bicycle," 15 July 2014. [Online]. Available: <https://grabcad.com/library/concord-selecta-12-bicycle-1>.
- [6] D. Koeppel, "Flight of the Pigeon," *Bicycling*, pp. 60-66, January 2007.
- [7] B. Lolek, "Bike Brake Caliper," GRABCAD, 24 October 2015. [Online]. Available: <https://grabcad.com/library/old-type-bike-brake-caliper-1>. [Accessed 23 September 2015].
- [8] "Frames and Materials," Exploratorium, [Online]. Available: <http://www.exploratorium.edu/cycling/frames1.html>. [Accessed 23 September 2015].
- [9] "MatWeb Material Property Data," Matweb, [Online]. Available: www.matweb.com. [Accessed 23 September 2015].
- [10] X. Zhongxia, T. Guan, X. Wen, G. Xin and Y. Xiaoran, "Load on Bicycle Frame During Cycling with Different," *Transactions of Tianjin University*, vol. 17, no. 4, pp. 270-274, 2011.
- [11] S. A. Kautz and M. L. Hull, "A Theoretical Basis for Interpreting the Force Applied to the Pedal in Cycling," *Biomechanics*, vol. 26, no. 2, pp. 155-165, 1993.
- [12] I. L. Silva, "GrabCAD," 14 September 2011. [Online]. Available: <https://grabcad.com/library/brazil-electric-bike-frame>. [Accessed 6 December 2015].
- [13] G. A. S. Morris Levy, "Effectiveness of vibration damping with bicycle suspension systems," *Sports Engineering*, vol. 8, no. 2, pp. 99-106, 2005.
- [14] J. Brandt, *The Bicycle Wheel*, Palo Alto: Avocet, Inc..
- [15] "Emulsion Polymerised Styrene Butadiene Rubber," AZO Materials, [Online]. Available: <http://www.azom.com/properties.aspx?ArticleID=1844>. [Accessed 23 September 2015].
- [16] Aerospace Specifications Metals Inc., [Online]. Available: <http://asm.matweb.com/search/SpecificMaterial.asp?bassnum=MA7075T6>. [Accessed 21 September 2015].